

## Karin cluster formation by asteroid impact

David Nesvorný<sup>a,\*</sup>, Brian L. Enke<sup>a</sup>, William F. Bottke<sup>a</sup>, Daniel D. Durda<sup>a</sup>, Erik Asphaug<sup>b</sup>,  
Derek C. Richardson<sup>c</sup>

<sup>a</sup> Department of Space Studies, Southwest Research Institute, 1050 Walnut St., Suite 400, Boulder, CO 80302, USA

<sup>b</sup> Earth Sciences Department, University of California, 1156 High St., Santa Cruz, CA 95064, USA

<sup>c</sup> Department of Astronomy, University of Maryland, College Park, MD 20742-2421, USA

Received 19 August 2005; revised 14 March 2006

Available online 2 May 2006

### Abstract

Insights into collisional physics may be obtained by studying the asteroid belt, where large-scale collisions produced groups of asteroid fragments with similar orbits and spectra known as the asteroid families. Here we describe our initial study of the Karin cluster, a small asteroid family that formed  $5.8 \pm 0.2$  Myr ago in the outer main belt. The Karin cluster is an ideal ‘natural laboratory’ for testing the codes used to simulate large-scale collisions because the observed fragments produced by the 5.8-Ma collision suffered apparently only limited dynamical and collisional erosion. To date, we have performed more than 100 hydrocode simulations of impacts with non-rotating monolithic parent bodies. We found good fits to the size–frequency distribution of the observed fragments in the Karin cluster and to the ejection speeds inferred from their orbits. These results suggest that the Karin cluster was formed by a disruption of an  $\approx 33$ -km-diameter asteroid, which represents a much larger parent body mass than previously estimated. The mass ratio between the parent body and the largest surviving fragment, (832) Karin, is  $\approx 0.15$ – $0.2$ , corresponding to a highly catastrophic event. Most of the parent body material was ejected as fragments ranging in size from yet-to-be-discovered sub-km members of the Karin cluster to dust grains. The impactor was  $\approx 5.8$  km across. We found that the ejection speeds of smaller fragments produced by the collision were larger than those of the larger fragments. The mean ejection speeds of  $>3$ -km-diameter fragments were  $\approx 10$  m s<sup>-1</sup>. The model and observed ejection velocity fields have different morphologies perhaps pointing to a problem with our modeling and/or assumptions. We estimate that  $\sim 5\%$  of the large asteroid fragments created by the collision should have satellites detectable by direct imaging (separations larger than 0.1 arcsec). We also predict a large number of ejecta binary systems with tight orbits. These binaries, located in the outer main belt, could potentially be detected by lightcurve observations. Hydrocode modeling provides important constraints on the interior structure of asteroids. Our current work suggests that the parent asteroid of the Karin cluster may have been an unfractured (or perhaps only lightly fractured) monolithic object. Simulations of impacts into fractured/rubble pile targets were so far unable to produce the observed large gap between the first and second largest fragment in the Karin cluster, and the steep slope at small sizes ( $\approx 6.3$  differential index). On the other hand, the parent asteroid of the Karin cluster was produced by an earlier disruptive collision that created the much larger, Koronis family some 2–3 Gyr ago. Standard interpretation of hydrocode modeling then suggests that the parent asteroid of the Karin cluster should have been formed as a rubble pile from Koronis family debris. We discuss several solutions to this apparent paradox.

© 2006 Elsevier Inc. All rights reserved.

*Keywords:* Asteroids; Collisional physics

### 1. Introduction

Our understanding of the Solar System’s past and present evolution relies, in large part, on numerical codes that are able to simulate outcomes of large-scale collisions (e.g., Benz and

Asphaug, 1994). These numerical codes are used in a variety of problems including planetary accretion (e.g., Agnor and Asphaug, 2004; Leinhardt and Richardson, 2004), formation of planetary and asteroid satellites (Canup and Asphaug, 2001; Canup, 2004; Durda et al., 2004), collisional evolution of asteroids (Durda et al., 1998; Bottke et al., 2005), formation of asteroid families (Michel et al., 2001, 2002, 2003, 2004), and impact cratering (e.g., Asphaug et al., 1996). The numerical

\* Corresponding author. Fax: +1 303 546 9687.

E-mail address: [davidn@boulder.swri.edu](mailto:davidn@boulder.swri.edu) (D. Nesvorný).

codes, however, are limited in important ways, particularly by the difficulty to define appropriate failure modes for various materials (see Holsapple et al., 2002).

Insight into the collisional physics may be obtained by studying the asteroid belt where numerous collisions have influenced the distributions of sizes and spins of asteroids, and have led to heavily cratered surfaces as evidenced by spacecraft imaging. Asteroid families are probably the most useful structures in the asteroid belt for studying large-scale impacts. An asteroid family is a group of asteroids with similar orbits and spectra that was produced by a collisional breakup of a large parent body (Hirayama, 1918). About fifty families have been identified in the asteroid belt to date (Zappalà et al., 1994, 2002; Nesvorný et al., 2005). Most of these families are ancient which makes it difficult to separate the effects of secondary collisions and dynamical evolution of family members via thermal effects from the state produced by the original impact (e.g., Marzari et al., 1995; Bottke et al., 2001).

We have recently identified several asteroid families with formation ages  $<10$  Myr (Nesvorný et al., 2002, 2003). These families represent nearly pristine examples of ejected fragments produced by disruptive asteroid collisions, because the observed remnants of recent breakups have apparently suffered limited dynamical and collisional erosion (Nesvorný and Bottke, 2004; Bottke et al., 2005). Studies of the families may help us to obtain important insights into the physics of large-scale collisions and may also validate the numerical codes used in other applications listed above.

Recently formed asteroid families may also help us to get important insights into our understanding of asteroid interiors. Disruptions of monolithic, fractured and ‘rubble-pile’ objects produce characteristic and distinct size–frequency distributions (SFDs) of debris (e.g., Michel et al., 2003, 2004). Therefore, clues to the interior structure of asteroids may be obtained by a careful comparison of the results of impact experiments/simulations with the SFDs of observed large fragments.

Here we report the results of our initial study of the asteroid breakup that led to the formation of the Karin cluster, a  $\sim 5.8$  Myr old main-belt asteroid family located at  $\sim 2.866$  AU (Nesvorný et al., 2002; Fig. 1). Our analysis is in many ways similar to that used by Michel et al. (2003, 2004).

Michel et al. (2003, 2004) were breakthrough works on this subject. These authors originally proposed that the parent body of the Karin cluster was a fractured/rubble pile asteroid. We believe this conclusion is not supported by the most recent observational data (Nesvorný and Bottke, 2004). We know now that the second largest fragment used by Michel et al., (4507) 1990 FV, is in fact a background asteroid with no relation whatsoever to the recent breakup (Nesvorný and Bottke, 2004). Once this body is removed, a large gap opens between the size of the largest fragment in the Karin cluster,  $\approx 17$ -km-diameter (832) Karin, and smaller fragments that have an extremely steep SFD slope ( $\approx 6.3$  differential power index). Simulation results reported by Michel et al. (2003, 2004) for fractured/rubble pile targets do not produce these characteristics.

Interestingly, Michel et al.’s simulations with (unfractured) monolithic parent bodies produced SFDs of fragments which

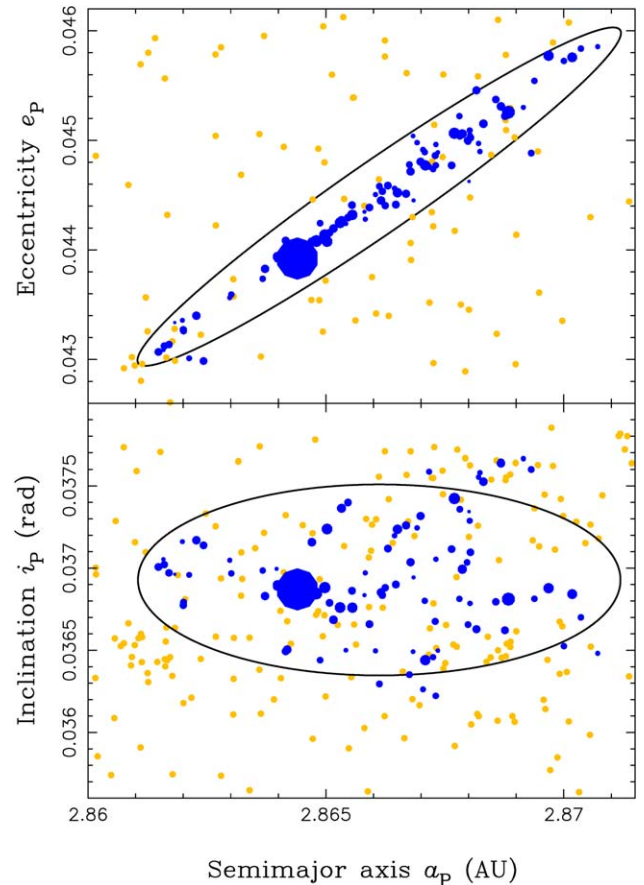


Fig. 1. Proper orbital elements of ninety Karin cluster members: (a)  $a_p$ ,  $e_p$ , and (b)  $a_p$ ,  $i_p$ . The size of each blue symbol is proportional to the diameter of a cluster member. Golden dots indicate the background bodies in the Koronis family. The black ellipses show the proper orbital elements of test bodies launched with  $15 \text{ ms}^{-1}$  speed from  $a_p = 2.8661$  AU,  $e_p = 0.04449$  and  $i_p = 0.03692$ , assuming  $f = 30^\circ$ , and  $\omega + f = 45^\circ$ , where  $f$  and  $\omega$  are the true anomaly and perihelion argument of the parent body. Figure from Nesvorný and Bottke (2004).

show a large gap between the sizes of the largest and smaller fragments. These SFDs are more similar to the revised SFD of the Karin cluster and may indicate that the disrupted asteroid was in fact a monolith. Unfortunately, Michel et al. reported only five simulations for monolithic parent bodies (all with a 24.5-km diameter; Nesvorný et al., 2002). This small number of tests makes it difficult to draw firm conclusions about the size and interior structure of the disrupted asteroid from Michel et al.’s results alone. For this reason, we conducted a detailed study of the impact parameter space. Here we report results for monolithic parent bodies.

To date, we performed more than 100 simulations of impacts into unfractured, monolithic targets. Some of these simulations produced strikingly good matches to the observed SFD of the Karin cluster and to the magnitude of the ejection speeds that has been inferred from the observed orbits. Based on these results, we propose that the Karin cluster may have been produced by a disruption of a monolithic (or perhaps only lightly fractured) parent asteroid. We also determined that this asteroid had  $\sim 33$ -km diameter and represented a much larger parent-body mass than suggested by previous estimates [e.g.,

Nesvorný et al. (2002) estimated a  $\sim 25$ -km diameter of the parent body based on the debiased SFD of observed large members]. Most mass dispersed into space by this collision is apparently contained in  $< 1$ -km-sized fragments.

We describe our method in Section 2, test it in Section 3, present results and their comparison with observations in Section 4. We discuss the results in Section 5.

## 2. Method

We divided the impact and post-impact evolution into three stages and used three different tools to follow the evolution of the system in each phase (see also Durda et al., 2004):

- Stage 1: We used a Smooth-Particle Hydrodynamic code (SPH3D; Benz and Asphaug, 1995) to model the initial stage of the impact where processes like shock propagation, fracture and fragmentation determine the evolution of the system. The effects of gravity, other than the gravitational self-compression of the target, were neglected at this stage.
- Stage 2: We used an efficient  $N$ -body code (pkdgrav; Richardson et al., 2000) to track the gravitational re-accumulation of fragments in the phase following Stage 1. The code simulates the self-gravity and low-speed collisions between fragments.
- Stage 3: This stage follows the evolution of bodies from a few days after impact to times where most fragments leave the effective Hill sphere. The gravitational force of largest fragments and the solar gravity are the most important physical processes during this phase. Hence, we used an efficient, symplectic  $N$ -body code (SyMBA; Duncan et al., 1998) to track the evolution of the system.

We describe these methods in more detail below. The method of coupling of the SPH calculations with a fast hierarchical  $N$ -body code (used here in Stages 1 and 2) was originally developed by Michel et al. (2001, 2002).

### 2.1. Stage 1

We modeled the initial stages of impacts between two asteroids with the 3D SPH code SPH3D (Benz and Asphaug, 1995). SPH3D is a Lagrangian code that solves the mass, momentum and energy conservation equations. It models shock propagation in elastic solids, utilizing a plastic yield criterion for intense deformation together with an explicit fracture and dynamic fragmentation model acting on the principal tensile component of the stress tensor during brittle deformation. We adopt fracture parameters appropriate for terrestrial basalt (Asphaug et al., 2002). The equation of state used is that of Tillotson (1962), which is based upon the linear relationship between shock and particle speeds (Melosh, 1989). The Tillotson equation of state gives excellent results in comparison to ejecta speeds derived from laboratory impact experiments (Benz and Asphaug, 1994, 1995). Comparison simulations using the ANEOS equation of state (Michel et al., 2003, 2004) have shown that for collisions

that do not include significant phase transitions, the details of the equation of state do not matter much.

The code ignores gravity because the time scale for shock propagation through the body and fragmentation is much shorter than the gravitational time scale (Asphaug, 1997). We incorporate gravitational self-compression of the target during the impact phase as an overburden stress that must be exceeded before fracture can initiate (Asphaug and Melosh, 1993). The simulations were run for 100 real world seconds.

To model the target body we typically used 10,000, 100,000 or 200,000 SPH particles. The low resolution runs were used to explore the parameter space at low CPU cost. The high resolution runs were used to verify results obtained with 100,000 SPH particles. Tests of accuracy are described in Section 3. We found that 100,000 or more particles provide sufficient accuracy.

### 2.2. Stage 2

When the initial stage of fragmentation/damage is complete, the end states of the SPH models are handed off as the initial state for the  $N$ -body simulations, which follow the trajectories of fragments that interact with each other by gravity. We used a modified version of the cosmological  $N$ -body code pkdgrav (Stadel, 2001), described in Richardson et al. (2000) (also see Leinhardt et al., 2000; Leinhardt and Richardson, 2002). pkdgrav is a scalable, parallel tree code that is the fastest code available for this type of simulation. An unique feature of this code is the ability to rapidly detect and accurately treat low-speed collisions between particles. This allows for realistic modeling of the formation of rubble pile accumulations among ejected fragments. See Durda et al. (2004), Richardson et al. (2005) and Leinhardt and Richardson (2005a) for examples of recent applications of this code.

The tree component of the code provides a convenient means to reduce the computational cost. The code uses a second-order leapfrog scheme for the integration and computes gravity moments from tree cells to hexadecapole order. Particles are considered to be finite-sized hard spheres and collisions are identified during each time step using a fast neighbor search algorithm. Low-speed collisions between debris fragments are treated as mergers resulting in a new spherical particle of appropriate combined mass and equivalent diameter.

Different approximations for mergers of debris fragments were used by Michel et al. (2002). These tests showed that inelastic bouncing of colliding fragments may lead to somewhat shallower SFD of small fragments than that produced by fully inelastic collisions. It is difficult, however, to determine whether inelastic bouncing of fragments used by Michel et al.'s is an accurate parametrization of low-speed collisions unless these collisions are analyzed in detail (e.g., via SPH simulations). In this work, we adopt the simplest approximation where all collisions lead to perfect sticking of the colliding fragments.

We used a hierarchical 3D tree code (companion; Leinhardt and Richardson, 2005b) to search for bound pairs in the output. These data were used to estimate the number and properties of binary systems produced by an impact.

The  $N$ -body simulations were run with a 50-s time step to  $t = 17$  days after the impact (i.e., to 30,000 time steps). The time step is a small fraction (about 1/50th) of the relevant dynamical time defined as  $(G\rho)^{-1/2}$ , where  $G$  is the gravitational constant and  $\rho$  is the particle density. We found that the reaccumulation in the late stages ( $t \gtrsim 8$  days) was minimal.

To convert the SPH3D output into input parameters for `pkdgrav`, we adopted several approximations. First, the SPH particles were converted into the hard-sphere particles utilized in `pkdgrav`. We ensured that the mass was conserved and used density  $\rho = 2.7 \text{ g cm}^{-3}$  to calculate the radius. Second, we merged all SPH particles that overlap. When the merger takes place, we use the conservation of mass and volume to produce the new SPH particle that is then converted into the `pkdgrav` particle. The velocity of the `pkdgrav` particle is equal to that of the corresponding SPH particle. We used a cutoff on density of SPH particles to detect extended SPH distributions representing vapor. These low-density SPH particles were ignored at the transition to the `pkdgrav` because of their generally small mass.

### 2.3. Stage 3

During the initial phases of debris cloud expansion, most fragments are still deep in the effective Hill sphere of the largest fragment, making it possible to neglect the gravitational effects of the Sun. To estimate the time when the gravity of the Sun starts to be important, we calculated the mean distance,  $\langle r \rangle$ , of the 100 largest fragments from the largest body and determined its evolution with time. We then compared  $\langle r \rangle$  to the Hill radius,  $r_H = a(\mu/3)^{1/3}$ , where  $a = 2.866 \text{ AU}$ ,  $\mu = m_{\text{lr}}/m_{\text{Sun}}$ , and where  $m_{\text{lr}}$  is the mass of the largest fragment and  $m_{\text{Sun}}$  is the mass of the Sun.

We then hand off the state of the system from `pkdgrav` to SyMBA (Duncan et al., 1998; Levison and Duncan, 2000) when  $\langle r \rangle \sim 0.5r_H$ , which typically happens about 6–10 days after the impact. This value of  $\langle r \rangle$  was chosen for the following reasons: (i) The effects of solar tides are negligible for  $r \lesssim 0.5r_H$ , making it possible to ignore solar gravity in simulations with `pkdgrav`; (ii) The effect of reaccumulation is minimal for  $t > 6$ –10 days after impact because the cloud of debris is already dispersed in a large space volume; (iii) The small fragments produced by the breakup generally have larger  $v_{\text{ej}}$  than large fragments (see Section 4.2). For this reason, at  $t \sim 6$ –10 days, small fragments are dispersed in a large volume making it possible to neglect the effects of their gravity on the trajectories of the largest surviving fragments. This allows us to speed up the calculation by tracking only the trajectories of several hundreds of gravitationally interacting large fragments. This allowed us to run many Stage-3 simulations with different impact locations/orientations in the Sun-centered reference frame.

SyMBA is a symplectic integrator that has the desirable properties of the sophisticated and highly efficient numerical algorithm known as Wisdom–Holman Map (WHM; Wisdom and Holman, 1991) and that, in addition, can handle close encounters (Duncan et al., 1998). This technique is based on a variant

of the standard WHM, but it handles close encounters by employing a multiple time step technique (Biesiadecki and Skeel, 1993). When bodies are well separated, the algorithm has the speed of the WHM method, and whenever two bodies suffer a mutual encounter, the time step for the relevant bodies is recursively subdivided.

We follow the trajectories of self-gravitating largest fragments from within the Hill sphere to distances where their behavior is controlled by solar gravity. The resulting orbits are converted back to ejection velocities using Gauss’ equations (see below). We then compare these values with the original ejection velocities. This procedure allows us to determine the effect of collective interactions in late stages of debris evolution and the validity of the usual Gauss-equation-based procedure to derive ejection velocities from the observed orbital parameters of an asteroid family.

## 3. Tests

### 3.1. Reproducibility

To test the reproducibility of our results, we ran several simulations twice on different processors. We also used different step sizes and changed error control parameters. We found that the results were almost exactly the same. This means the results of our simulations are reproducible when the initial parameters of the impact are the same.

### 3.2. Dependence on SPH resolution

We tested the dependence of our results on SPH resolution by: (i) performing several simulations with exactly the same impact parameters except for the target’s diameter, which we changed by  $\sim 1 \text{ cm}$  between individual runs, and (ii) varying the number of SPH particles between 10,000 and 200,000.

Results from (i) with only 10,000 SPH particles showed significant variability. The diameters of the 1st and 2nd largest fragments varied by as much as  $\approx 1 \text{ km}$  and  $\approx 2 \text{ km}$ , respectively, between individual runs. This variability was suppressed when 100,000 particles were used. With 100,000 particles,  $d_{1\text{st}}$  and  $d_{2\text{nd}}$  fluctuated only by  $\approx 0.2 \text{ km}$  and  $\approx 0.7 \text{ km}$ , respectively, and were similar to values obtained in our experiments with 200,000 SPH particles. This is an indication of an improved convergence of results when  $\gtrsim 100,000$  particles are used. We also found a similar dependence on resolution when comparing the momentum imparted in the largest escaping fragments.

While encouraging, these tests are inconclusive because the number of SPH particles may not have been varied sufficiently. W. Benz (personal communication) has conducted similar tests of convergence of the SPH code in the regime of laboratory impacts. By using up to 2,240,000 SPH particles he showed that the size of the largest fragment may vary when different numbers of SPH particles are used. He attributed these results to the fact that the average explicit fracture threshold increases with the number of particles.

It is not clear whether our code may suffer from the same problem. The tests of W. Benz described above do not include

Stage 2 where the size of the largest fragment increases by reaccumulation of fragments. Moreover, uncertainties in the albedo values of Karin cluster members (discussed below) appear to be more important than the effects of the SPH resolution.

#### 4. Results

The non-rotating targets were assumed to be spherical and were composed of unfractured, monolithic basalt with a density of  $2.7 \text{ g cm}^{-3}$ . We used spherical basalt impactors. To set up the SPH simulation, we selected the target and impactor sizes,  $d_{\text{tar}}$  and  $d_{\text{imp}}$ , respectively, the impact speed,  $v_{\text{imp}}$ , and the impact angle,  $\theta$ . We performed more than 100 simulations with different  $d_{\text{tar}}$ ,  $d_{\text{imp}}$ ,  $v_{\text{imp}}$  and  $\theta$ . These simulations were divided into five classes:

- Class 1: nominal case with  $v_{\text{imp}} = 5 \text{ km s}^{-1}$  and  $\theta = 45^\circ$ .
- Class 2: low-speed impact case with  $v_{\text{imp}} = 3 \text{ km s}^{-1}$  and  $\theta = 45^\circ$ .
- Class 3: high-speed impact case with  $v_{\text{imp}} = 7 \text{ km s}^{-1}$  and  $\theta = 45^\circ$ .
- Class 4: nearly head-on impacts with  $v_{\text{imp}} = 5 \text{ km s}^{-1}$  and  $\theta = 15^\circ$ .
- Class 5: oblique impacts with  $v_{\text{imp}} = 5 \text{ km s}^{-1}$  and  $\theta = 75^\circ$ .

According to Bottke et al. (1994),  $v_{\text{imp}} = 5 \text{ km s}^{-1}$  is roughly the mean collision speed between main belt asteroids. Collisions with  $v_{\text{imp}} = 3 \text{ km s}^{-1}$  and  $v_{\text{imp}} = 7 \text{ km s}^{-1}$  are about 30% and 50% less likely, respectively, than a collision with  $v_{\text{imp}} = 5 \text{ km s}^{-1}$ . Also, (832) Karin has  $\approx 4.1 \text{ km s}^{-1}$  rms collision speed with the main belt asteroids (intrinsic collision probability  $P_i \approx 4 \times 10^{-18} \text{ km}^{-2} \text{ yr}^{-1}$ ). Therefore, values of  $v_{\text{imp}}$  used here span the interesting range of impact speeds.

The rate of collisions with  $\theta$  is proportional to  $\sin \theta$ . Thus, collisions with  $\theta = 75^\circ$  and  $\theta = 15^\circ$  are about 40% more and 60% less likely, respectively, than a collision with  $\theta = 45^\circ$ . This argument cannot be used to favor grazing impacts as the most likely collision geometries for the Karin cluster formation because high-probability near-grazing impacts on a target body can produce catastrophic breakups only if the impactor is big. Because the number of relevant-size asteroid impactors in the main belt strongly decreases with  $d$ , however, catastrophic near-grazing impacts are relatively rare compared to those with smaller  $\theta$ .

We performed simulations in each class with many different  $d_{\text{tar}}$  and  $d_{\text{imp}}$ . First, we selected  $d_{\text{tar}}$  and  $d_{\text{imp}}$  using a trial and error method and comparing our results to the size-distribution of the Karin cluster. In all cases except for Class-2 parameters, we were able to find an acceptable fit after 4 to 7 test simulations. The outcomes of low-speed Class-2 impact simulations are sensitive to small changes in  $d_{\text{tar}}$  and/or  $d_{\text{imp}}$ , which makes it difficult to converge toward a desired solution.

In the second step, we have run exploratory, low-resolution simulations with 10,000 SPH particles to test the behavior of the SFD for impact parameters near the solution found above. This effort helped us establish the envelope of values that may provide good fits to the observed SFD. For example, the best

solution for Class 1 found above is  $d_{\text{tar}} = 30 \text{ km}$  and  $d_{\text{imp}} = 5 \text{ km}$ . Hence, we used  $d_{\text{tar}} = 26, 28, \text{ and } 32 \text{ km}$  and  $d_{\text{imp}} = 4.0, 4.5, 5.0, 5.5 \text{ and } 6.0 \text{ km}$  in step two, 20 simulations in total.

We analyzed these low-resolution results and selected the initial parameters for high-resolution simulations (100,000 SPH particles) that were designed to map the interesting part of the parameter space. The simulation outcomes with impact parameters that provided the best matches to the observational data were selected for further analysis, including additional 200,000-SPH-particle simulations, a detailed comparison of the ejection velocity fields, search for binaries, and discussion of the rotation of the largest fragment. We describe these results below.

Our best-fit solutions to the observed parameters of the Karin cluster are not unique because we explore only five representative planes in the four-dimensional space of parameters ( $d_{\text{tar}}$ ,  $d_{\text{imp}}$ ,  $v_{\text{imp}}$ , and  $\theta$ ). Moreover, we limited our initial study of this problem to spherical, monolithic, basaltic, and non-rotating targets and impactors. Other setups, including different assumptions on the interior structure of the parent body, rotating targets, low-density C-type impactors, etc., will be described in forthcoming papers.

#### 4.1. Size–frequency distribution

##### 4.1.1. Observed SFD

The size–frequency distribution (SFD) of the Karin cluster is shown in Fig. 2. We used 90 members selected by Nesvorný and Bottke (2004) from a catalog of  $\sim 220,000$  asteroid orbits. Given the restrictive criterion for membership used by

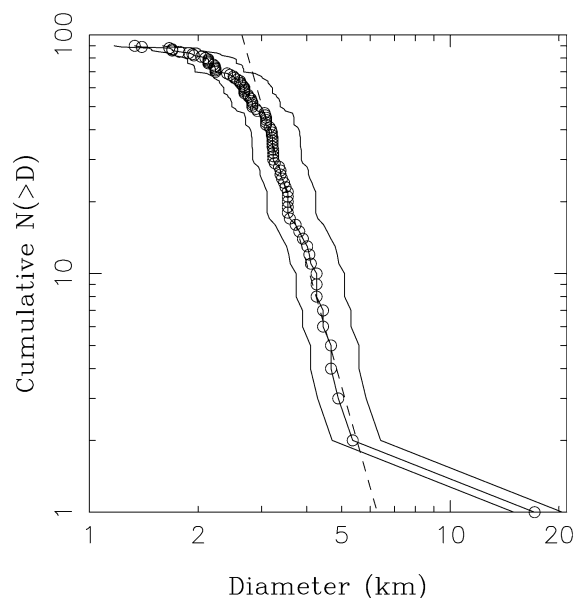


Fig. 2. The cumulative size–frequency distribution of Karin cluster members identified in Nesvorný and Bottke (2004). Absolute magnitudes listed in the Minor Planet Center catalog were converted into diameters using albedo  $p_V = 0.2$ ; each individual member’s diameter is labeled by a circle. The best-fit power index to the slope between 3 and 5.5 km diameters is  $\sim 5.3$  (dashed line). This very steep slope changes for diameter  $< 3 \text{ km}$  due to the observational incompleteness. Left and right solid lines show SFDs that we obtained with  $p_V = 0.26$  and  $p_V = 0.14$ , respectively.

Nesvorný and Bottke very few of these asteroids should be interlopers. Also, given the young age of the family, we assume that: (i) secondary fragmentation events among the original fragments did not change the SFD of diameter  $d > 1$  km members in significant ways (Bottke et al., 2005), and (ii) the orbits and spins of the fragments were not modified in important ways by the Yarkovsky and YORP effects (Nesvorný and Bottke, 2004). Therefore, these asteroid fragments present a clear-cut case of debris distribution produced by a disruptive collision between asteroids.

To determine the size of an object from the absolute magnitude,  $H$ , we need to know its visual albedo,  $p_V$ . Unfortunately, albedo values of Karin cluster members are unknown. To estimate these values, we used the fact that the parent body of the Karin cluster was an S-type member of the Koronis family (Jedicke et al., 2004; Nesvorný et al., 2003, 2005). The SIMPS catalog (Tedesco et al., 2002) lists albedo values for 24 Koronis family members. Their mean albedo is  $0.198 \pm 0.012$ . The rms variation is 0.061, illustrating the large spread of albedo values in the Koronis family. To account for this uncertainty, we used  $p_V = 0.14, 0.2$  and  $0.26$  as three possible values of albedo for the Karin cluster members.  $p_V = 0.2$  is our nominal case,  $p_V = 0.14$  and  $p_V = 0.26$  were chosen to span the rms variation in the Koronis family.

Corresponding to  $H = 11.18$ , the diameter of (832) Karin is 17.1 km for  $p_V = 0.2$ . It is 15.0 km for  $p_V = 0.26$  and 20.5 km for  $p_V = 0.14$ . Similarly, the second largest fragment, (13907) 1998 XE13, has  $H = 13.7$  and the mean, minimal and maximal diameters  $d_{2nd} = 5.4, 4.7$  and 6.4 km, respectively.

Our sample of Karin cluster members is observationally incomplete. This is clearly seen at the transition from  $d > 3$  km, where the observed SFD is characterized by a steep slope, to  $d < 2$  km, where very few Karin cluster members are known (Fig. 2). We did not try to debias the sample because that would require that we make several non-trivial assumptions about the efficiency of observational surveys. Instead, we used only members with  $d > 3$  km for which the effects of incompleteness are less severe.

We assumed that the cumulative size distribution,  $N(> d)$ , can be locally described by a power law,  $N(> d) \propto d^{-\alpha}$ , with the best-fit  $\alpha$  found by the least-squares method. The best fits to the observed distribution between 3- and 5.4-km diameters (for  $p_V = 0.2$ ) occurs for  $\alpha = 5.3 \pm 0.5$ .

With  $p_V = 0.2$ , the total volume of 90 fragments corresponds to a sphere with a  $\approx 20$  km diameter. Assuming a 20-km-diameter parent body,  $m_{lr}/m_{pb} \sim 0.63$ , suggesting a sub-catastrophic event. In fact, we will show below that  $m_{lr}/m_{pb} \approx 0.15$ – $0.2$ , corresponding to a highly catastrophic impact, with a large fraction of the parent body hiding in small fragments beyond the observational detection limit.

#### 4.1.2. Model SFDs

With  $v_{imp} = 3 \text{ km s}^{-1}$  and  $\theta = 45^\circ$  (Class 2 impacts), we did not find  $d_{tar}$  and  $d_{imp}$  values that would produce a SFD similar to that observed in the Karin cluster (2). This probably means that these parameter choices are unlikely to match the constraints. We also noticed that the momentum imparted into

the large fragments by our Class-2, low-speed impacts is generally much larger than the one inferred from observations of the Karin cluster (see Section 4.2.2). Consequently, the ejection speeds are too large. Given these results, we find it unlikely that Class-2, low-speed impacts might produce reasonable analogs for the Karin cluster. We will not discuss low-speed impacts further in this paper.

Fig. 3 shows the result of our fifteen 100,000-SPH-particle simulations of Class-3 impacts ( $v_{imp} = 7 \text{ km s}^{-1}$  and  $\theta = 45^\circ$ ). To cope with uncertainties in  $p_V$ , we have spread these simulations in parameter space to produce fragments that are as small as 15.2 km and as large as 20.0 km. The red regions in Fig. 3 correspond to values of  $d_{tar}$  and  $d_{imp}$  that produce good matches to the observed SFD. A good match is defined here as one producing  $15.0 \leq d_{lr} \leq 20.5$  km (panel a),  $4.7 \leq d_{2nd} \leq 6.4$  km, where  $d_{2nd}$  is the diameter of the second largest fragment (panel b), and  $4.6 \leq \alpha \leq 5.8$  (panel c). The mean ejection speed (panel d) will be discussed in Section 4.2

Fig. 4 shows an example of a Class-3 simulation where we have obtained a good match to the observed SFD (Table 1). The initial parameters of this simulation were  $d_{tar} = 33$  km and  $d_{imp} = 5.75$  km (denoted by star in Fig. 3). The largest surviving fragment has  $d = 17.0$  km (to be compared to observed  $d = 17.1$  km for  $p_V = 0.2$ ), the second largest fragment has  $d = 4.8$  km (compare to observed  $d = 5.4$  for  $p_V = 0.2$ ), the power index,  $\alpha$ , of the cumulative sized distribution,  $N(> d) \propto d^{-\alpha}$ , is  $\approx 5.3$  (compare to observed  $\alpha = 5.3 \pm 0.5$ ).

The best fits to the size of the largest fragment occur along a diagonal area in  $d_{tar}$  and  $d_{imp}$  space (Fig. 3a). Apparently, a larger impactor is needed for a larger target body to produce observed  $d_{lr} \approx 17$  km. The linear dependence between  $d_{tar}$  and  $d_{imp}$  may be empirically described by  $d_{imp}^* = 4.6 \text{ km} + 0.33(d_{tar} - 30 \text{ km})$ . Impactors that are significantly larger than  $d_{imp}^*$  for fixed  $d_{tar}$  produce  $d_{lr}$  that are too small, and vice versa.

It is possible to match  $d_{lr}$  over a large range of  $d_{tar}$  but a more limited range of  $d_{tar}$  produces good matches to both  $d_{lr}$  and  $d_{2nd}$ . Fig. 3b illustrates this result. To match  $d_{2nd}$ ,  $d_{imp}$  needs to be between  $\approx 4.5$  and  $\approx 6$  km (for a basaltic,  $\rho = 2.7 \text{ g cm}^{-3}$ , Class-3 impactor). If the impactor's diameter is larger than  $\approx 6$  km, model  $d_{2nd}$  becomes significantly larger than the observed  $d_{2nd} \approx 5.4$  km. If  $d_{imp} < 4.5$  km, model  $d_{2nd}$  becomes significantly smaller than observed  $d_{2nd}$ . The range of plausible  $d_{tar}$  corresponding to  $4.5 \lesssim d_{imp} \lesssim 6$  km is  $29 \lesssim d_{tar} \lesssim 35$  km.

A tighter range of  $d_{tar}$  values is required to match the observed SFD's slope (Fig. 3c). In general, the model slopes are shallower than those observed. The model SFD's slope index exceeds  $\alpha \approx 4.8$  for only a special combination of  $d_{tar}$  and  $d_{imp}$ . Most steep slopes occur for  $31 \lesssim d_{tar} \lesssim 34$  km, with  $d_{tar} \approx 33$  km and  $d_{imp} \approx 5.8$  km producing best fits to observed  $\alpha \approx 5.3$ .

These results are encouraging. We were able to identify one possible set of impact parameters that produces a satisfactory match to the observed SFD (see Fig. 4). These parameters are:  $d_{tar} \approx 33$  km,  $d_{imp} \approx 5.8$  km,  $v_{imp} \approx 7 \text{ km s}^{-1}$  and  $\theta \approx 45^\circ$ . Moreover, we will show below that the magnitude of the ejection speeds inferred from observations can be also fit by using

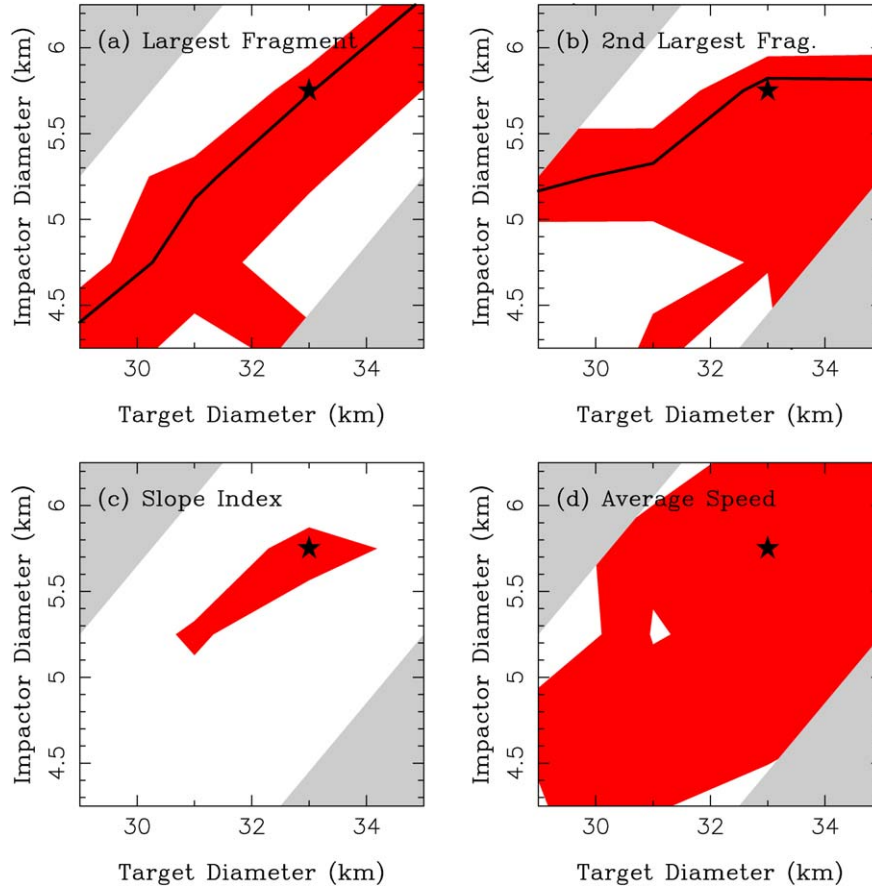


Fig. 3. Location of good model fits to the Karin cluster as a function of target and impactor diameters for  $v_{\text{imp}} = 7 \text{ km s}^{-1}$  and  $\theta = 45^\circ$  (our Class-3 impact simulations). A good fit (denoted in red) is defined here as the one producing  $15.0 \leq d_{\text{lr}} \leq 20.5 \text{ km}$  (a),  $4.7 \leq d_{2\text{nd}} \leq 6.4 \text{ km}$  (b),  $4.6 \leq \alpha \leq 5.8$  (c), and  $9.8 \leq \langle v_{\text{ej}} \rangle \leq 16.8 \text{ m s}^{-1}$  (d), where mean speed ( $\langle v_{\text{ej}} \rangle$ ) was calculated as the average over ejection speeds of the 2nd to 90th largest fragments with respect to the 1st largest fragment. The solid lines in (a) and (b) denote Class-3 simulations with  $d_{\text{tar}}$  and  $d_{\text{imp}}$  that produce  $d_{\text{lr}} = 17.1 \text{ km}$  and  $d_{2\text{nd}} = 5.4 \text{ km}$ , which are the estimated sizes of the largest and second largest members of the Karin cluster for  $p_V = 0.2$ . The place where these two lines cross (near the location of star) is where the best fits were obtained for  $p_V = 0.2$ . The SFD for  $d_{\text{tar}}$  and  $d_{\text{imp}}$  denoted by the star is shown in Fig. 4. Shaded regions were not sampled.

the model parameters described above. Taken together, our results indicate that the parent body of the Karin cluster could have been a  $d \approx 33\text{-km}$  monolithic asteroid that collided with a high-speed,  $d \approx 5.8\text{-km}$  impactor. We will discuss this result and its implications in more detail in Section 5.

The best results of our Class-1 simulations ( $v_{\text{imp}} = 5 \text{ km s}^{-1}$  and  $\theta = 45^\circ$ ) occur for  $d_{\text{tar}} \approx 30 \text{ km}$  and  $d_{\text{imp}} \approx 5 \text{ km}$ . These simulations typically produce  $d_{\text{lr}}$  and  $d_{2\text{nd}}$  that are in the same ballpark as the observed values. Interestingly, these simulations produce shallow SFD slopes with  $\alpha \lesssim 4$  that are incompatible with  $\alpha = 5.3 \pm 0.5$  inferred from observations. This may be explained by one or more of the following reasons: (i) We may not have sampled parameter space sufficiently with our twenty 10,000 and ten 100,000 SPH particle simulations in Class 3; other (non-sampled) combinations of  $d_{\text{tar}}$  and  $d_{\text{imp}}$  could produce steeper slopes. (ii)  $v_{\text{imp}} \approx 5 \text{ km s}^{-1}$  impacts generally produce shallower slopes than impacts with higher  $v_{\text{imp}}$ . If (ii) applies, a high-speed collision may better explain the SFD of the Karin cluster than  $v_{\text{imp}} = 5 \text{ km s}^{-1}$ . Further work will be needed to resolve this issue.

The best result for Class-1 impacts was obtained with  $d_{\text{tar}} = 32 \text{ km}$  and  $d_{\text{imp}} = 5 \text{ km}$ . This simulation produced  $d_{\text{lr}} =$

$18.5 \text{ km}$ ,  $d_{2\text{nd}} = 6.2 \text{ km}$  and  $\alpha = 4.2$  (Table 1). Except for a slightly shallower slope, the fit to the observed SFD is good (Fig. 5).

Fig. 6 illustrates the difficulty in fitting the observed distribution with Class-4 impacts ( $\theta = 15^\circ$ ; nearly head-on impacts). We were able to find impact parameter values that produce correct sizes for the 1st and 2nd largest fragments in the Karin cluster but incorrect distribution at small  $d$ . In Fig. 6, the model SFD does not sharply increase from  $d_{2\text{nd}} \sim 5.4 \text{ km}$  as the observed SFD but instead continues with a shallow slope to  $d \sim 2.8 \text{ km}$ , where it has an inflection point. This behavior is typical for all nearly head-on impacts that produce desired values of  $d_{\text{lr}}$  and  $d_{2\text{nd}}$ . For this reason, we believe that the Karin cluster was more likely produced by an impact with larger  $\theta$ .

The best result for Class-4 impacts was obtained with  $d_{\text{tar}} = 28 \text{ km}$  and  $d_{\text{imp}} = 4 \text{ km}$ . This simulation produced  $d_{\text{lr}} = 16.6 \text{ km}$ ,  $d_{2\text{nd}} = 4.8 \text{ km}$  and  $\alpha = 4.7$  (Table 1). The model SFD, however, suffers from the same problem as the one shown in Fig. 6, where model fragments are smaller than the observed ones for  $d < 5 \text{ km}$ .

Our Class-5 simulations ( $\theta = 75^\circ$ ; oblique impacts) require larger impactors than more centered impacts to produce the ob-

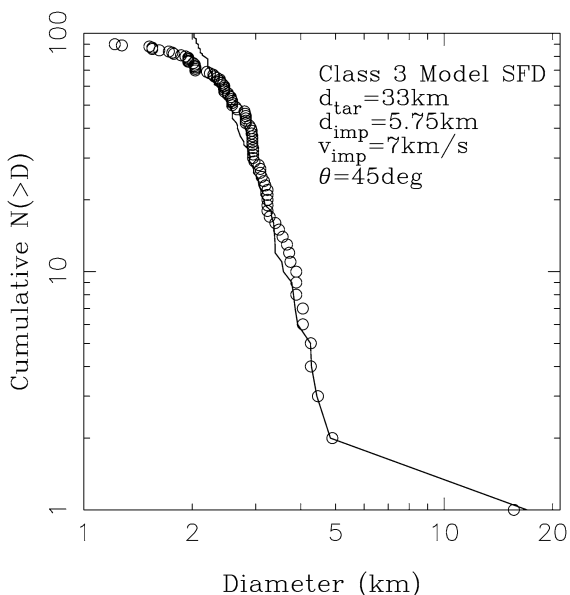


Fig. 4. Example of a good model fit to the observed size–frequency distribution that we obtained for  $d_{\text{tar}} = 33$  km,  $d_{\text{imp}} = 5.75$  km,  $v_{\text{imp}} = 7$  km s<sup>-1</sup> and  $\theta = 45^\circ$ . The observed (for  $p_V = 0.24$ ) and model SFDs are denoted by circles and a line, respectively. For smaller  $p_V$ , the observed SFD would shift slightly to the right (see Fig. 2) and would require a slightly larger  $d_{\text{tar}}$  and  $d_{\text{imp}}$ .

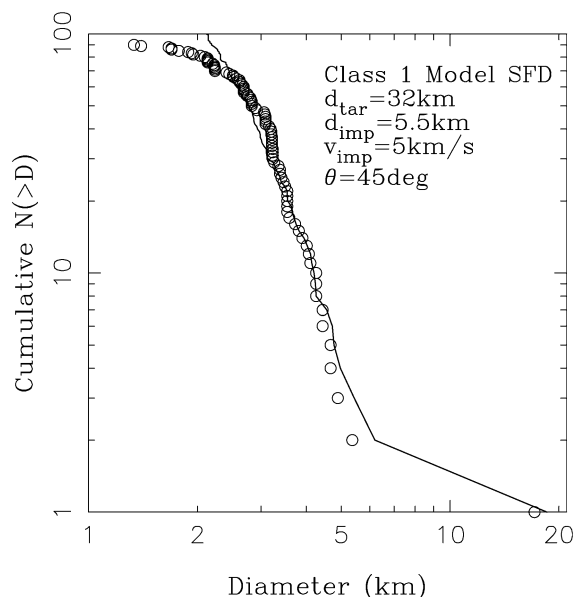


Fig. 5. Example of a model fit to the observed size–frequency distribution that we obtained for  $d_{\text{tar}} = 32$  km,  $d_{\text{imp}} = 5.5$  km,  $v_{\text{imp}} = 5$  km s<sup>-1</sup> and  $\theta = 45^\circ$ . The observed (for  $p_V = 0.2$ ) and model SFDs are denoted by circles and a line, respectively. The model SFD is slightly shallower than the observed one for  $3 < d < 6$  km.

Table 1  
Impact parameters and results for three selected simulations

	(obs.)	(1)	(2)	(3)
$d_{\text{tar}}$ (km)		32	<b>33</b>	28
$d_{\text{imp}}$ (km)		5.5	<b>5.75</b>	4.0
$v_{\text{imp}}$ (km s <sup>-1</sup> )		5	<b>7</b>	5
$\theta$ (°)		45	<b>45</b>	15
$d_{1r}$ (km)	17.1	18.5	<b>17.1</b>	16.6
$d_{2\text{nd}}$ (km)	5.4	6.2	<b>4.8</b>	4.8
$\alpha$	5.3	4.2	<b>5.3</b>	4.7
$m_{1r}/m_{\text{pb}}$		0.19	<b>0.14</b>	0.21
$v_{1r}$ (m s <sup>-1</sup> )		10.5	<b>6.9</b>	5.0
$\langle v_{\text{ej}} \rangle$ (m s <sup>-1</sup> )	12.7	10.1	<b>11.2</b>	10.0

*Notes.* The rows are: diameter of the target body ( $d_{\text{tar}}$ ); diameter of the impactor ( $d_{\text{imp}}$ ); impact speed ( $v_{\text{imp}}$ ); impact angle ( $\theta$ ); diameter of the largest fragment ( $d_{1r}$ ); diameter of the second largest fragment ( $d_{2\text{nd}}$ ); cumulative SFD slope index ( $\alpha$ ); largest remnant to parent body mass ratio ( $m_{1r}/m_{\text{pb}}$ ); post-impact speed of the largest remnant ( $v_{1r}$ ); and the mean ejection speed of the 2nd to 90th largest fragments with respect to the largest fragment ( $\langle v_{\text{ej}} \rangle$ ). The columns show: (obs.) values obtained from observations; (1) Class 1 simulation with  $d_{\text{tar}} = 32$  km and  $d_{\text{imp}} = 5.5$  km; (2) Class 3 simulation with  $d_{\text{tar}} = 33$  km and  $d_{\text{imp}} = 5.75$  km; (3) Class 4 simulation with  $d_{\text{tar}} = 28$  km and  $d_{\text{imp}} = 4.0$  km. Observed quantities were derived from orbits and sizes of ninety Karin cluster members with  $f = 30^\circ$ ,  $\omega + f = 50.5^\circ$  and  $p_V = 0.2$ . Our preferred model parameters and results are denoted in bold.

served  $d_{\text{tar}}$  and  $d_{\text{imp}}$  values. For example,  $d_{\text{tar}} = 27.5$  km and  $d_{\text{imp}} = 9$  km produce SFDs that have roughly the correct values of  $d_{1r}$  and  $d_{2\text{nd}}$ , and a steep, slightly concave distribution at small  $d$ . We have two reasons, however, to believe that an oblique impact is a less likely scenario for the origin of the Karin cluster. First, the likelihood of an impact of an  $\approx 9$ -km-diameter asteroid is  $\sim 5$ – $10$  times less likely than an impact of an  $\approx 5$ -km-diameter asteroid because smaller asteroids are more abundant in the main belt than the larger ones (Bottke et al.,

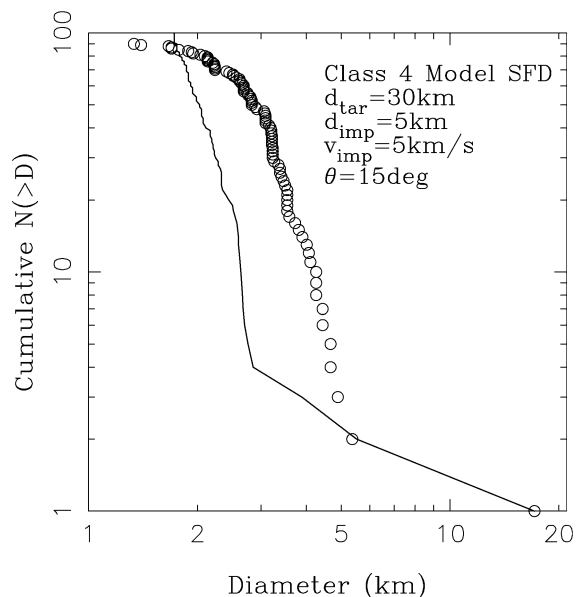


Fig. 6. Example of a model SFD that we obtained for  $d_{\text{tar}} = 30$  km,  $d_{\text{imp}} = 4.5$  km,  $v_{\text{imp}} = 5$  km s<sup>-1</sup> and  $\theta = 15^\circ$ . The observed (for  $p_V = 0.2$ ) and modeled SFDs are denoted by circles and a line, respectively. The model distribution fits very well the sizes of 1st and 2nd largest fragments but fails to produce the observed SFD at small  $d$ .

2005). Second, the ejection speeds of fragments produced by oblique impacts are substantially larger than the observed ones (see next section). This happens because only a small part of the target and impactor bodies overlap along the impact path. Therefore, there is less opportunity to convert the kinetic energy of the impactor into other energy forms. Also, for oblique impacts, the impactor material typically contributes to the mass of the second largest fragment.

## 4.2. Ejection velocity

### 4.2.1. $v_{ej}$ deduced from observations

The ejection velocity of fragments may be determined from the observed distribution of proper orbital elements of Karin cluster members. We assume that the proper elements have not significantly changed over the family's age. Indeed, given the young age of the Karin cluster, the effects thermal forces and gravitational encounters with large asteroids are negligible in the current context (Nesvorný and Bottke, 2004).

We used Gauss equations (e.g., Murray and Dermott, 1999, p. 54) to relate the orbital elements of a Karin cluster member ( $a_p$ ,  $e_p$  and  $i_p$ ) to the components of its ejection velocity,  $\hat{v}_{ej}$ , along the direction of the orbital motion,  $v_t$ , in the radial direction,  $v_r$ , and perpendicular to the orbital plane,  $v_w$ :

$$\begin{aligned} \delta a/a &= \frac{2}{na(1-e^2)^{1/2}} [(1+e \cos f)\delta v_t + (e \sin f)\delta v_r], \\ \delta e &= \frac{(1-e^2)^{1/2}}{na} \left[ \frac{e+2 \cos f+e \cos^2 f}{1+e \cos f} \delta v_t + (\sin f)\delta v_r \right], \\ \delta i &= \frac{(1-e^2)^{1/2}}{na} \frac{\cos(\omega+f)}{1+e \cos f} \delta v_w. \end{aligned} \quad (1)$$

Here,  $\delta a = a_p - a_{ref}$ ,  $\delta e = e_p - e_{ref}$  and  $\delta i = i_p - i_{ref}$ , where  $a_{ref}$ ,  $e_{ref}$  and  $i_{ref}$  define a reference orbit, and  $f$  and  $\omega$  are the true anomaly and the perihelion argument of the disrupted parent body at the instant of the impact.

A natural reference frame for our impact simulations is the one fixed at the target body. Unfortunately, it is difficult to use this frame for the observed fragments without a priori knowledge of the impact parameters. We therefore use a different frame which can be easily defined for both the SPH-derived and observed velocities. In our SPH simulations, we fix the reference frame at the largest surviving fragment and calculate the velocities of smaller fragments with respect to the largest fragment. To determine ejections velocities from the observed orbits, we use  $a_{ref} = 2.8644$  AU,  $e_{ref} = 0.043921$  and  $i_{ref} = 2.11203^\circ$ , corresponding to (832) Karin, and calculate  $v_t$ ,  $v_r$  and  $v_w$  from inverted Eq. (1).

The transformation from  $a$ ,  $e$ ,  $i$  to  $v_t$ ,  $v_r$ ,  $v_w$  depends on the true anomaly,  $f$ , and the argument of perihelion,  $\omega$ , of the reference orbit. The exact values of these parameters are unknown. From the tilt of the distribution in  $a$ ,  $e$  (Fig. 1), it has been suggested that  $|f| \lesssim 30^\circ$  (Nesvorný et al., 2002). We experimented with  $f = 10^\circ$  and  $f = 30^\circ$ . Values of  $f < 10^\circ$  produce ejection velocity fields with unrealistically large  $v_t$ .

The value of  $\omega$  is not constrained unless we make explicit assumptions about the ejection velocity field. For example, isotropic ejection velocity fields produce the observed distribution of orbits if  $|\omega + f| \lesssim 45^\circ$  or  $|\omega + f + 180^\circ| \lesssim 45^\circ$  (Nesvorný et al., 2002). In Eq. (1),  $\delta i \propto v_w \cos(\omega + f)$ . We used  $\omega + f = \arccos\langle \cos(\omega + f) \rangle = 50.5^\circ$ , where  $\langle \cos(\omega + f) \rangle$  is the average over randomly distributed  $\omega$ . The inferred values of  $v_w$  would be about 1.5 times smaller if  $\omega + f \sim 0^\circ$  or  $180^\circ$  and much larger if  $\omega + f \sim 90^\circ$  or  $270^\circ$ . We believe that  $\omega + f \sim 90^\circ$  or  $270^\circ$  did not occur because  $v_w$  would be much larger than  $v_t$  and  $v_r$ . None of our Karin impact experiments to

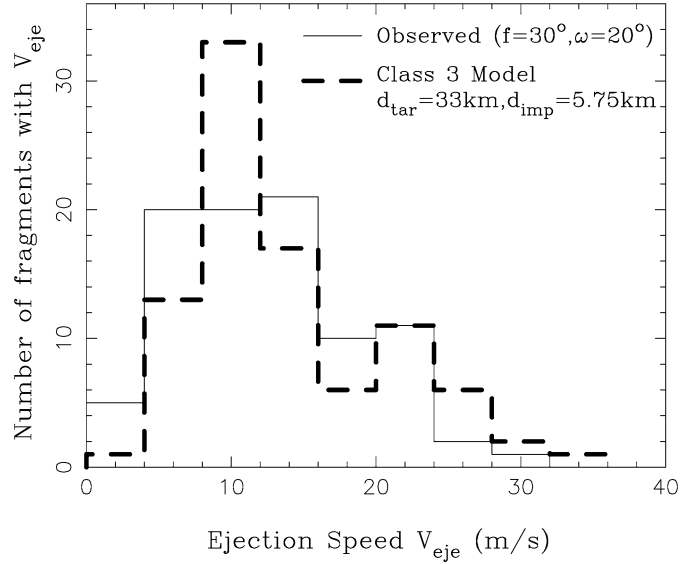


Fig. 7. Histogram of the ejection speed distribution inferred from observations (thin solid line) and the one obtained as a result of our Class-3 simulation with  $d_{tar} = 33$  km,  $d_{imp} = 5.75$  km,  $v_{imp} = 7$  km s $^{-1}$  and  $\theta = 45^\circ$  (Fig. 4). In both cases, ejection speeds of second to 90th largest fragments with respect to the largest fragment are shown. The ejection speeds determined from observed orbits were inferred using  $f = 30^\circ$  and  $\omega = 20^\circ$  and Eq. (1).

date have yet yielded a velocity component that is significantly larger than the other two.

With  $f = 30^\circ$  and  $\omega + f = 50.5^\circ$ , the mean ejection speed of the 2nd to 90th largest fragments with respect to the 1st largest fragment, is  $\langle v_{ej} \rangle = 12.7$  m s $^{-1}$ . The distribution of ejection speeds is broadly shaped with values of  $v_{ej}$  between 0 and 26 m s $^{-1}$  (with exception of (51923) 2001 QD95 which has  $v_{ej} \sim 31$  m s $^{-1}$ ) (Fig. 7). There exists a clear correlation between the mean ejection speed and size of a fragment, with smaller fragments having, on average, larger ejection speeds. The mean ejections speeds for diameter 2–3, 3–4, and 4–5 km are 13.3, 12.2, and 8.8 m s $^{-1}$ , respectively. With  $f = 10^\circ$  and  $\omega + f = 50.5^\circ$ , and with  $f = 30^\circ$  and  $\omega + f = 70^\circ$ ,  $\langle v_{ej} \rangle \approx 18$  m s $^{-1}$ . With  $f < 10^\circ$  and/or  $\omega + f = 70^\circ$ , the mean ejection speed exceeds 20 m s $^{-1}$ .

We used a 3D visualization tool to understand the morphology of the ejection velocity field inferred from orbits and its dependence on  $f$  and  $\omega$ . With  $f = 30^\circ$  and  $\omega + f = 50.5^\circ$ , the velocity field is asymmetric with respect to the largest fragment. The envelope of the velocity field is best described as an irregular 3D structure with characteristic size of  $\sim 20$  m s $^{-1}$  in all directions. None of the velocity components is significantly higher than the other two. Most fragments have positive  $v_t$  and  $v_r$ . With  $f = 10^\circ$  and  $\omega + f = 70^\circ$ , the ejection velocity field becomes stretched in  $v_r$  and  $v_w$  directions.

### 4.2.2. Model $v_{ej}$

The mean ejection speed for our Class-3 simulation with parameters described in Fig. 4 is 11.2 m s $^{-1}$  (average over 2nd to 90th largest fragment's speeds in the frame fixed at the largest fragment). This value is similar to that inferred from observations, 12.7 m s $^{-1}$ , for  $f = 30^\circ$  and  $\omega + f = 50.5^\circ$ . The mean

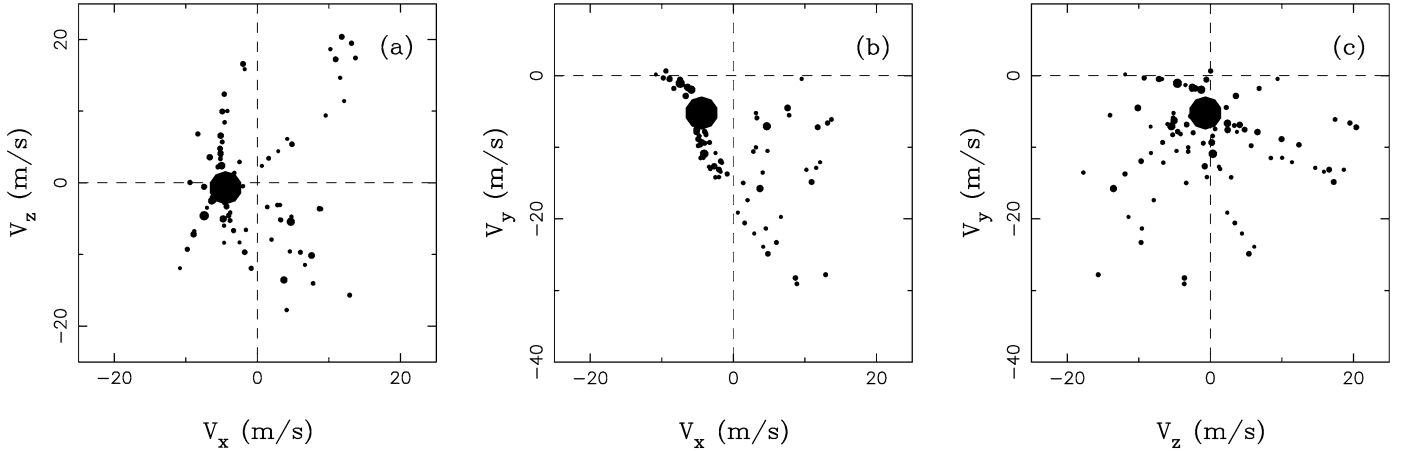


Fig. 8. The ejection velocities of hundred largest fragments produced by our Class-3 simulation with  $d_{\text{tar}} = 33$  km,  $d_{\text{imp}} = 5.75$  km. Panels show three different projections of  $\hat{v}_{\text{ej}}$ . The size of a symbol is proportional to the fragment's diameter. In this experiment, the target with  $v_x = 0$ ,  $v_y = 0$ ,  $v_z = 0$  was impacted at a  $45^\circ$  angle by a projectile with  $v_x = -7$  km s $^{-1}$  and  $v_y = 0$ ,  $v_z = 0$ . Accordingly, the impact produced negative  $v_x$  and  $v_y$  of the largest fragment. Characteristic rays that resemble the rays of larger craters on the Moon can be seen in panels (a) and (c).

ejections speeds for diameter 2–3, 3–4, and 4–5 km are 12.3, 10.7, and 7.6 m s $^{-1}$ , respectively, which is also in good agreement (slightly lower) with the observed values (13.3, 12.2, and 8.8 m s $^{-1}$  for  $f = 30^\circ$  and  $\omega + f = 50.5^\circ$ ; see previous section). This shows that our Class-3 simulations are able to predict the correct magnitude of the ejection speeds and the size-ejection speed correlation observed in the Karin cluster.

Similarly good agreement between magnitudes of the model and observed speeds exists for simulations in Classes 1 and 4 (Table 1). Conversely, Class-2 and Class-5 impacts (low impact speed and oblique impacts) produce ejection speeds in excess of 20 m s $^{-1}$ . These ejection speeds cannot be ruled out a priori because of the uncertainty produced by unknown  $f$  and  $\omega + f$ . Yet, combined with our difficulties to produce correct SFD with Class-2 and Class-5 parameters, and the large  $d_{\text{imp}}$  required in Class 5 (see Section 4.1.2), we believe that these impact parameters (low  $v_{\text{imp}}$  and/or large  $\theta$ ) are unlikely.

All simulations conducted here produced ejection velocity fields with characteristic morphology (Fig. 8). For  $\theta = 15^\circ$  and  $\theta = 45^\circ$ , the distribution of  $\hat{v}_{\text{ej}}$  is a flat, warped structure that is nearly perpendicular to the velocity vector of the largest fragment. The individual ejection velocity vectors are distributed non-randomly in the disk forming nearly radial rays that resemble the rays of large craters on the Moon. Oblique impacts produce velocity field morphologies that are more bowl-shaped. Conversely, the velocity field inferred from Karin members' orbits is generally a more isotropic, 3D structure (Section 4.2.1).

We can think of several ways to explain the difference between the morphologies of the model and observed velocity fields. One possibility is that our estimate of  $f$  and  $\omega$  is incorrect. If  $f \sim 0^\circ$  and  $\omega + f \sim 90^\circ$ , the ejection velocity field inferred from the observations would become more similar to the simulated one. Moreover, 2002 CX104, 1994 EX, 2000 UV4, (40510) 1999 RU87 could form a ray in velocity space like the ones produced in our simulations. Another option is that our modeling may be missing some important component of debris evolution. For example, the solar gravity may modify

the velocity field of escaping fragments in the later stages of the debris cloud's expansion.

To test this possibility, we have performed a series of Phase-3 simulations (see Section 2.3). To set up the initial conditions these simulations, we used the distributions of fragments at time  $t \approx 8$  days after impact, when some particles are still deep within the effective Hill sphere of the largest fragment. For example, for our preferred Class-3 impact parameters ( $d_{\text{tar}} = 33$  km and  $d_{\text{imp}} = 5.75$  km), the mean distance at  $t = 8$  days of the 100 largest fragments from the largest fragment is  $\approx 8000$  km. This turns out to be about  $r_{\text{H}}/2$ , where  $r_{\text{H}} \approx 16,000$  km is the Hill radius of a  $d \approx 17$  km largest fragment at 2.865 AU (assuming  $2.7$  g cm $^{-3}$  density).

At  $t \approx 8$  days, we include the Sun's gravity in the simulation and track the evolution of fragments to times where most large fragments become separated by several of their effective Hill radii. The gravitational attraction between the large fragments and solar gravity determines the final orbits. We then use the Gauss equations [Eq. (1)] to map the final orbits back to ejection velocities and compare them with the original velocity field like that shown in Fig. 8. The integration method is described in Section 2.3.

We found that in a few instances typical for fragments that have barely enough speed to escape from the largest fragment, solar perturbations can be important. In general, however, the ejection velocity field is well represented by our Phase 2 simulations and is not substantially modified by Sun's gravity. This result can be explained by comparing the ejection speeds of fragments with the Hill velocity,  $v_{\text{H}} = v_{\text{K}}/2(\mu/3)^{1/3} \approx 0.3$  m s $^{-1}$ , where  $v_{\text{K}}$  is the Kepler velocity. Because the ejection speeds are typically at least one order in magnitude larger than  $v_{\text{H}}$ , we conclude, in agreement with our Phase 3 results, that the solar gravity should not modify the velocity field of fragments in important ways (at least for Karin-cluster forming impacts). We discuss other, more plausible options that may explain the difference between model and observed velocity fields in Section 5.

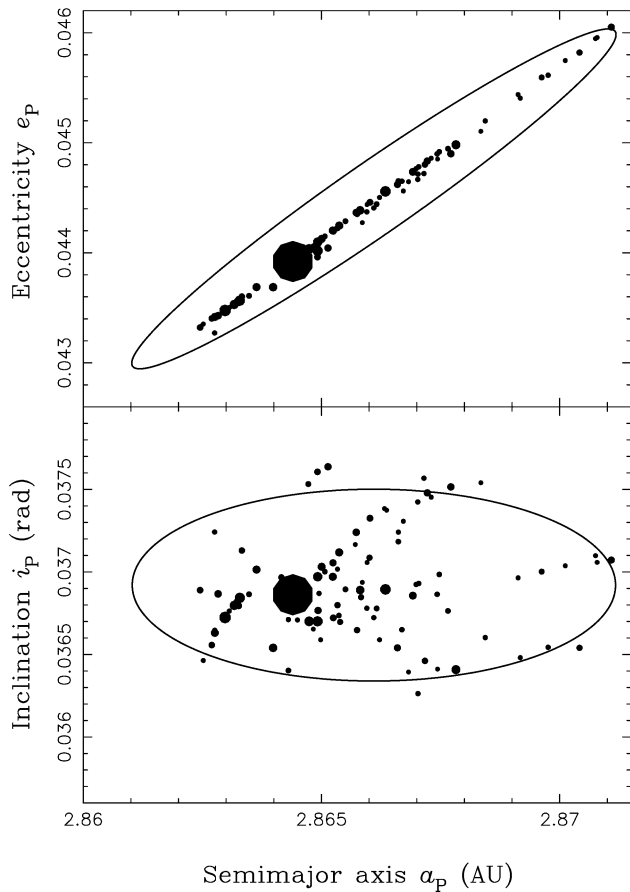


Fig. 9. The orbits of largest fragments produced by an impact experiment defined by  $d_{\text{tar}} = 33$  km,  $d_{\text{imp}} = 5.75$  km,  $v_{\text{imp}} = 7$  km s $^{-1}$ ,  $\theta = 45^\circ$ ,  $f = 10^\circ$  and  $\omega + f = 50.5^\circ$ . The size of a symbol is proportional to the fragment's diameter. The impact was set to occur along  $\hat{r}$  direction. This model result shows a remarkable similarity to the distribution of observed orbits of Karin cluster members (see Fig. 1).

To set up a Phase 3 simulation, we must choose  $f$ ,  $\omega$  and the orientation of the impact in the heliocentric reference frame. By varying these parameters, we found that impacts along the radial direction (roughly perpendicular to both the normal to the orbital plane and the orbit velocity vector) can best explain the orbits of the Karin cluster. For this orientation, the reference frame of the SPH/pkdgrav simulations ( $\hat{x}$ ,  $\hat{y}$ ,  $\hat{z}$ ; impact occurring along  $\hat{x}$  and toward negative  $x$ ; target hit at positive  $y$  and  $z = 0$ ) coincides with a local orbital frame defined by  $\hat{r}$ ,  $\hat{t}$ ,  $\hat{w}$ , where  $\hat{r}$ ,  $\hat{t}$ ,  $\hat{w}$  are radial, tangential and orbit-normal vectors at the instant of impact.

Fig. 9 illustrates a result of one such impact experiment. In this figure, the largest fragment is offset toward smaller  $a$  with respect to the center of the family in the same way (832) Karin is offset from the center of the Karin cluster (Fig. 1). This happens because  $v_y$  of the largest fragment is negative (see Fig. 8b). Therefore,  $v_r$  is also negative due to the choice of the impact orientation in the orbital frame, and  $\delta a < 0$  from Gauss equations [Eq. (1)]. The largest fragment is more symmetrically placed in  $i$  with respect to other fragments because its  $v_z \approx 0$  (see Fig. 8a). Together, these impact conditions create the desired effect where the appearance of the synthetic family

in  $a$ ,  $e$ ,  $i$  (Fig. 9) looks very similar to that of the observed Karin cluster (Fig. 1).

The impact orientation discussed above is not unique. Impacts along  $v_t$  may also produce a good match to observations. These impacts between main belt asteroids, however, are much less likely than those along  $v_r$  (Bottke et al., 1994). Impacts along  $v_w$  direction produce an asymmetric position of the largest fragment in proper inclination which is not observed. Thus, we believe impacts along  $v_w$  can be ruled out.

#### 4.3. Binary formation

Hydrocode simulations show that a large number of initial binaries can be produced among escaping ejecta by an asteroid collision (so-called Escaping Ejecta Binaries or EEBs; see Durda et al., 2004). Our expectation was that a very young family like the Karin cluster might have a significantly higher frequency of EEBs than the background because satellites may not yet been removed by subsequent impacts or long-term gravitational perturbations. To our surprise, Merline et al. (2004a), using Hubble Space Telescope (HST) observations, have not found a binary in the Karin cluster out of 17 imaged, small family members (832 Karin was not imaged).

To determine the number of initial binaries produced by our SPH simulations, we used a hierarchical 3D tree code (companion; see Section 2.2) to search for bound pairs in the output at  $t = 17$  days after impact. In the following, we describe the result obtained with our preferred Class 3 simulation ( $d_{\text{tar}} = 33$  km,  $d_{\text{imp}} = 5.75$  km,  $v_{\text{imp}} = 7$  km s $^{-1}$ ,  $\theta = 45^\circ$ ). Other simulations that fit the size–frequency and velocity distributions of Karin cluster members produce similar results.

Fig. 10 shows sizes of binary components and their orbits. In total, the simulation produced 717 EEBs (out of 72477 fragments), where the binary components were separated by more than 2 physical radii and less than 1 Hill radius of the primary. Binary systems with separations not in this range are dynamically unstable. Most of the selected, potentially long-lived binary pairs have semimajor axes smaller than 120 km and large eccentricities (denoted by diamonds in Fig. 10). These binary pairs are unlikely to be detected by HST imaging because of their small separations. A few binary pairs have large separations, including 4 pairs with  $a > 150$  km and primary/secondary component diameters ranging from 1.5/0.8 to 4.4/1.2 km. Binary systems like these could be potentially detected by Merline et al.'s HST search.

Fig. 11 shows the difference in the apparent visual magnitude between components of each EEB shown in Fig. 10 and their separation on the sky. Observations at opposition were assumed. In the same plot, we also show two satellite systems found in the Koronis family: (1) S/2003(22899)1 is about 1.5 km diameter (the size of Dactyl) and orbits (22899) (1999 TO14) at about 170 km (Merline et al., 2004b); and (2) S/2004(17246)1 is about 2 km diameter and orbits (17246) (2000 GL74) at about 230 km (Tamblyn et al., 2004). The primaries of both these systems have approximate diameter 4.5 km and the apparent visual magnitude at the time of observation of about 18.

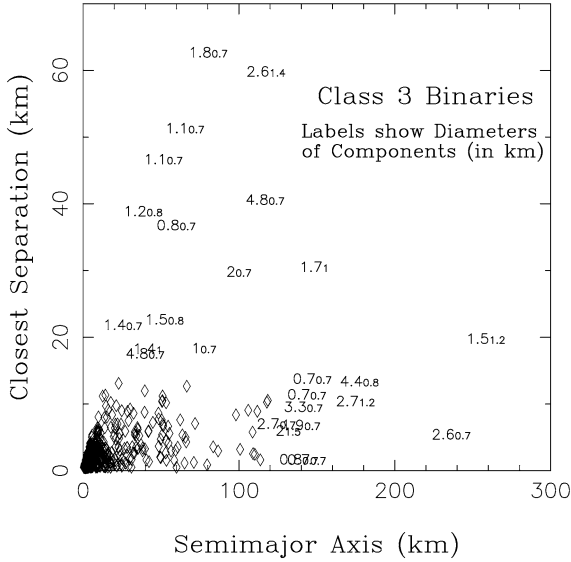


Fig. 10. The Escaping Ejecta Binaries produced in a single simulation with  $d_{\text{tar}} = 33$  km,  $d_{\text{imp}} = 5.75$  km,  $v_{\text{imp}} = 7$  km s $^{-1}$ ,  $\theta = 45^\circ$ . The labels show the diameters of the primary and secondary components in km (e.g., 4.80.7 stands for a binary pair with 4.8-km-diameter primary and 0.7-km-diameter secondary components). For clarity, numerous binary pairs with the semimajor axis smaller than 120 km and with the closest separation (i.e., pericenter) smaller than 15 km are denoted by diamonds.

These two binary systems serve us as a guide into what type of an EEB would be detected in the Karin cluster by HST. For example, five of our EEBs have a separation larger than 0.1 arcsec and magnitude difference smaller than 4. We believe that these systems could be detectable with HST. The primaries of these EEBs have diameters  $d > 2$  km. Because about 100 fragments produced by the impact exist in this size range, we estimate that roughly 1 out of 20 Karin cluster members with  $d > 2$  km should have a companion detectable by HST. This result may explain the lack of satellite detection in the Karin cluster by Merline et al. and Tamblin et al., who only imaged 17 objects. According to our estimated  $\approx 5\%$  frequency of potentially detectable satellites in the Karin cluster, their sample was apparently not large enough to guarantee a satellite discovery.

An interesting byproduct of our analysis is the large propensity of binaries on close orbits (Fig. 10). These satellites might be detected by lightcurve observations. Indeed, it has been proposed from the rate of satellite discovery by lightcurve observations of the main belt asteroids, that close satellites may exist around a relatively large fraction ( $> 5\%$ ) of main belt asteroids (P. Pravec, personal communication).

#### 4.4. Spin rates

Yoshida et al. (2004) found from lightcurve observations that the rotational period of (832) Karin is  $P = 18.35 \pm 0.02$  h. This slow rotation of the largest fragment in the Karin cluster is puzzling when compared to the model results described below.

Love and Ahrens (1997) determined the rotation speed of the largest fragment after an initially non-rotating target body suffered an impact. Love and Ahrens did not explicitly fol-

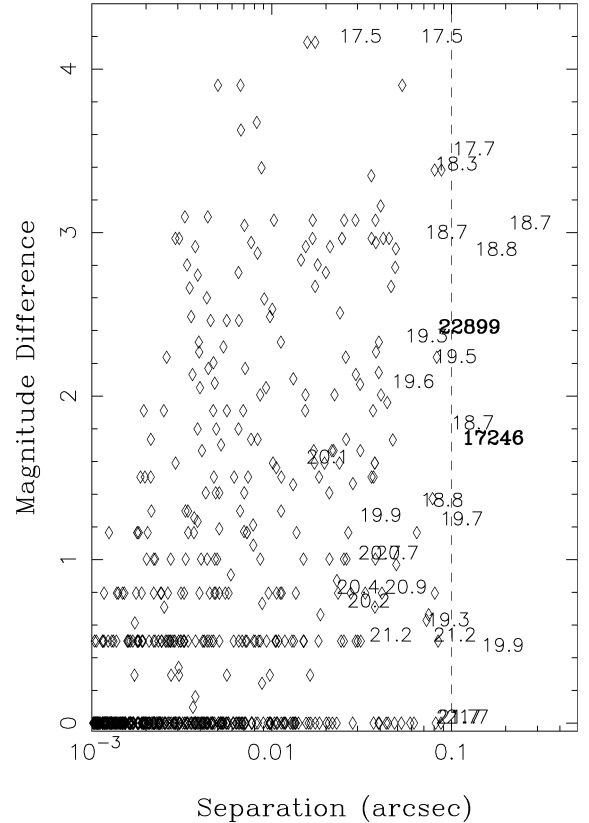


Fig. 11. The separation on the sky and magnitude difference for EEBs shown in Fig. 10. We assumed observations in the opposition and  $p_V = 0.2$  albedo. The labels show the apparent visual magnitude of the primary component. EEBs with  $a < 120$  km and  $a(1 - e) < 15$  km are denoted by diamonds. Also shown here are two satellites discovered by Merline et al. (2004b) and Tamblin et al. (2004) in the Koronis family: S/2003(22899)1 and (2) S/2004(17246)1. Primaries in these binary systems had the visual apparent magnitude of about 18 at the time of observation. The vertical dashed line is drawn at 0.1 arcsec. Five Karin cluster EEBs separated by more than 0.1 arcsec should be detectable by the HST (Merline et al., 2002).

low gravitational reaccumulation among the fragments but instead estimated the rotation speed from the angular momentum of the bound swarm of debris immediately after the impact. The impact parameters from their runs that are most closely match our best fit parameters are: 31.6-km-diameter target, 5-km-diameter projectile, 5 km s $^{-1}$  impact speed, and 45 $^\circ$  impact angle. They obtained  $m_{\text{lr}}/m_{\text{pb}} = 0.12$ , which is close to our  $m_{\text{lr}}/m_{\text{pb}} = 0.19$  for our preferred Class-1 simulation setup [(1) in Table 1]. The spin period of the largest fragment estimated for this and similarly destructive impacts is  $\approx 3$  h, about six times shorter than  $P$  of (832) Karin inferred from observations. [Note that the YORP torque (Rubincam, 2000; Vokrouhlický et al., 2003) cannot despin an asteroid of the size of (832) Karin on a  $< 10$  Myr time scale.]

A problem with some of the results from Love and Ahrens (1997) may be that they based their calculation on considerations of the total angular momentum shortly after the impact when it is not exactly clear how the momentum will be distributed among the final fragments. To test this possibility, we tracked the evolution of the spin of the largest fragment during the reaccumulation phase to 17 days after impact. We found that  $P$

ranges between 6 and 30 h in different experiments. For our preferred Class-3 impact parameters, however,  $P < 10$  h, again much shorter than the one (832) Karin. Our model, however, is limited in important ways because it treats all collisions as inelastic mergers. Another problem may be that we have only considered non-rotating parent bodies; an impact with the right trajectory could have ‘stopped’ the original rotation. A more extensive modeling effort will be needed to systematically explore the effect of different parameters on the rotation rate of fragments.

Future results can be compared with the spin periods and obliquities of Karin cluster members (Sasaki et al., 2004, 2005; Yoshida et al., 2004; Nesvorný and Bottke, 2004). For example, Nesvorný and Bottke (2004) found that most large members of the Karin cluster are retrograde rotators. These additional constraints on impact conditions may help us to remove some uncertainty that we face due to the unknown geometry of the studied impact.

## 5. Discussion

To date, we performed  $>100$  simulations of impacts into unfractured, monolithic targets. Some of these simulations produced strikingly good matches to the observed size–frequency distribution of the Karin cluster and to the magnitude of the ejection speeds that has been inferred from the observed orbits. Conversely, impacts into fractured/rubble pile targets thus far did not produce reasonable fits to the SFD of the Karin cluster although limited number of simulations have been done (see below) (Michel et al., 2003, 2004). In particular, the impact simulations with fractured targets are unable to account for the large gap between the sizes of the 1st and 2nd largest fragments observed in the Karin cluster (Fig. 2), and produce SFDs that are much shallower than the observed one. Together, these results may suggest that the parent body of the Karin cluster was a monolithic (or perhaps only lightly fractured) asteroid rather than a (heavily) fractured/rubble pile body [see Richardson et al. (2002) for a definition of the internal structure corresponding to these terms].

These results are puzzling because the parent asteroid of the Karin cluster was produced by an earlier disruptive collision that created the much larger, Koronis family some  $\sim 2$  Gyr ago (Bottke et al., 2001; Nesvorný et al., 2002). [Note there is only  $\sim 0.3\%$  chance that the parent body of the Karin cluster was an interloper in the Koronis family (Migliorini et al., 1995).] It was estimated that the Koronis family formed by a collisional disruption of a  $\approx 160$ -km-diameter asteroid (Tanga et al., 1999). SPH3D/pkdgrav modeling then predicts that the large parent object was fractured into small pieces that were ejected and later reaccumulated in space into objects with a rubble-pile structure (Michel et al., 2001, 2002). Therefore, as pointed out above, the parent body of the Karin cluster should have reaccumulated from smaller debris some 2–3 Gyr ago. Yet, when hit by an impactor  $\approx 5.8$  Myr ago, it produced the SFD and ejection speeds characteristic of a disruption of a monolithic object (again based on SPH3D/pkdgrav modeling; Fig. 2 and Michel et al., 2003).

We can think of two solutions to this problem.

**Solution 1.** These results may suggest that the parent body of the Karin cluster somehow consolidated into a more coherent body from a gravitationally bound aggregate of rubble. For example, internal voids could have been partly filled by regolith by impact-induced seismic shaking (Richardson et al., 2004), and the regolith and fragmental breccias may have been lithified by mild or moderate impact-induced shocks (e.g., Scott and Wilson, 2005). It is not clear, however, whether these processes will affect the whole body or only its surface layers, because impact-induced shocks may not produce the required pressures ( $\sim 20$  GPa) across the asteroid interior.

**Solution 2.** Michel et al. (2003) reported only 5 simulations with fractured/rubble-pile 25-km-diameter targets. Given our experience with impacts into monolithic targets, we believe more experimenting may be necessary to determine how different impact parameters (target/projectile size, impact speed and angle, etc.) affect the results. Note, for example, that a 5.75-km-diameter projectile was needed to obtain our fit in Fig. 4, while Michel et al. used  $\leq 3$ -km-diameter impactors. It is also unclear how the internal size–frequency distribution of rubble-pile components affects the impact outcome.

These results will have important implications for our understanding of asteroid interiors. They may be placed in the context of other constraints on the interior structure of asteroids such as: (i) the Galileo and NEAR/Shoemaker spacecraft data on Eros, Mathilde and Ida (reviewed by Sullivan et al., 2002), (ii) meteoritical data [see Scott and Wilson (2005) for a discussion], (iii) asteroid densities (e.g., Britt et al., 2002; Hilton et al., 2002), and (iv) the new results on asteroid rotation (Holsapple, 2005). Interestingly, these data/results are consistent with a picture where km-sized and larger asteroids, including those produced by large scale collisions (like Ida which is a member of the Koronis family), are not rubble piles.

Another puzzling result that we obtained by experimenting with monolithic targets is related to the ejection velocity field of the fragments. While the magnitudes of the model ejection speeds nicely match the orbit distribution of Karin members, there is a significant difference between the morphology of the modeled and observed ejection velocity fields. The ejection fields obtained in our simulations are highly anisotropic 2D structures with characteristic rays that resemble the rays of large craters on the Moon. The velocity field inferred from Karin members’ orbits is more an isotropic, 3D structure.

Our modeling may be missing some important component of debris evolution: (i) the inelastic bouncing of fragments during the reaccumulation phase that lasts typically until several days after impact may be important means of randomizing the initial ejection field. [In this paper we assumed that colliding fragments always merge into a single spherical particle with the mass and velocity that are determined by the mass and momentum conservation.] (ii) The morphology of the ejection field may depend in critical ways on the interior structure of the target, and/or on its rotation prior to the impact. Alternatively, we may still be missing some other important effect perhaps related to the ways fractures propagate through the target, to details of

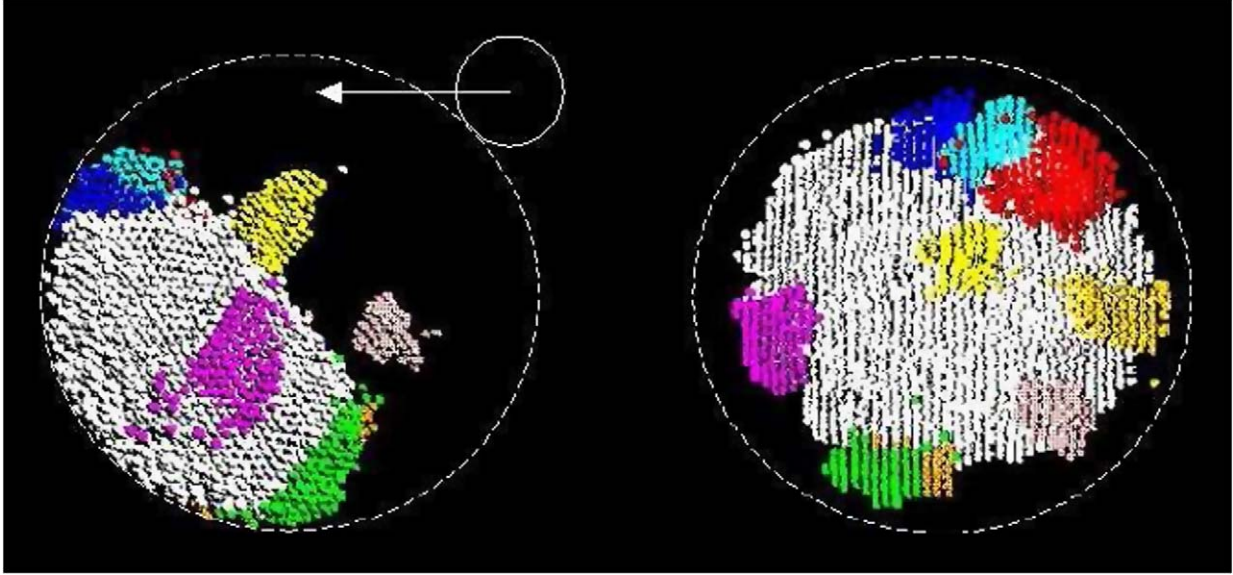


Fig. 12. The pre-impact location of the material distributed among the largest fragments. Left: side view; spherical target, impactor and impact direction are shown. Right: top view. We show the location of ten largest fragments produced by the impact simulation with  $d_{\text{tar}} = 33$  km,  $d_{\text{imp}} = 5.75$  km,  $v_{\text{imp}} = 7$  km s<sup>-1</sup> and  $\theta = 45^\circ$ . Different colors denote different fragments: (1) white, (2) red, (3) green, (4) magenta, (5) dark blue, (6) turquoise, (7) yellow, (8) grey, (9) gold and (10) light red, where the number in parenthesis identifies the fragment (1 is the 1st largest, 2 is the 2nd largest, etc.). To make this figure, we determined all mergers of the `pkdgrav` particles that produced  $n$ th largest fragment and show the location of the corresponding SPH particles before the impact.

the equation of state, etc. More experimenting will be needed to resolve these issues.

The largest fragments produced by our impact simulations are probably produced by a physical process similar to the one described by Melosh (1984). This process, known as spall, can be briefly described as follows.

The disturbance produced by the impact propagates away from the point of initial contact as a stress pulse of a large amplitude (a shock). The front side of the target is crushed to fragments the size of individual grains or smaller. The energy density in the stress wave declines both because of dilution (as it expands it is spread over a greater volume) and because of energy losses from inelastic processes in the wave. The stress wave interferes with its own tensile image as it reflects from the free surface boundary. Stresses are lower in the interference zone producing lower shock levels and larger fragments.

Fig. 12 illustrates the original locations of the largest fragments produced by the impact simulation with  $d_{\text{tar}} = 33$  km,  $d_{\text{imp}} = 5.75$  km,  $v_{\text{imp}} = 7$  km s<sup>-1</sup> and  $\theta = 45^\circ$ . It is clear from this figure that the largest fragments sample the rear hemisphere of the parent body. It is also interesting to find that each largest fragment represents material from a specific location. For example, one side of the largest fragment coincides with the surface on the rear side of the target body. The other side of the largest fragment samples the material that was originally deep in the interior.

This result may help to explain the recent spectroscopic observations of (832) Karin (Sasaki et al., 2004; Vernazza et al., 2005). Both these groups have found that the reflectance spectrum of this asteroid varies with its rotational phase. One side of (832) Karin looks ‘fresh’ showing deep absorption bands and shallow spectral slopes in infrared wavelengths; the other side is probably more ‘space-weathered’ and ancient [see, e.g., Clark

et al. (2002) and Chapman (2004) for reviews on space weathering]. It is tempting to identify these two faces of (832) Karin with the two sides of the largest fragment shown in Fig. 12. In this scenario, the ‘fresh’ side of (832) Karin would be composed from the rock that was excavated from the interior of the parent body only about  $\approx 5.8$  Myr ago. In addition, the coherent appearance of the largest fragments in Fig. 12 may also help to explain why Gaspra, Eros and Ida seem to have partially competent interiors (composed from fractured but intact rock materials) rather than being collections of gravitationally bound aggregates (rubble piles) (Sullivan et al., 2002).

These results, however, are at odds with the high degree of damage produced by the SPH code in all fragments. At face value, the SPH code shows that all fragments are completely damaged (by ‘completely damaged’ we mean here a fragment for which the material strength does not play an important role in its cohesive properties). If true, the shape of the fragments and their coherent appearance in Fig. 12 are misleading; without a cohesive strength these fragments will fall apart and re-assemble by gravitational reaccumulation at later times [as first proposed by Michel et al. (2001)]. This scenario would predict that surfaces of the final fragments represent a complex mixture of interior and near-surface rocks of the original object. Apparently, new observations and improved numerical codes will be needed to determine the exact degree of damage and role of reaccumulation in catastrophic collisions of asteroids.

## Acknowledgments

This paper is based upon work supported by the NSF under grant No. 0307926 and by the NASA under grant No. NAG-513038. Work by E. Asphaug was funded by the NASA PG&G grant entitled Small Bodies & Planetary Collisions. Research

funds for W. Bottke were provided by NASA's OSS program (grant NAG510658). D.C. Richardson was supported by NASA's OSS program (grant NAG511722).

## References

- Agnor, C., Asphaug, E., 2004. Accretion efficiency during planetary collisions. *Astrophys. J.* 613, L157–L160.
- Asphaug, E., 1997. Impact origin of the Vesta family. *Meteorit. Planet. Sci.* 32, 965–980.
- Asphaug, E., Melosh, H.J., 1993. The Stickney impact of PHOBOS—A dynamical model. *Icarus* 101, 144–164.
- Asphaug, E., Moore, J.M., Morrison, D., Benz, W., Nolan, M.C., Sullivan, R.J., 1996. Mechanical and geological effects of impact cratering on Ida. *Icarus* 120, 158–184.
- Asphaug, E., Ryan, E., Zuber, M., 2002. Asteroid interiors. In: Bottke, W.F., Cellino, A., Paolicchi, P., Binzel, P.R. (Eds.), *Asteroids III*. Univ. of Arizona Press, Tucson, pp. 463–484.
- Benz, W., Asphaug, E., 1994. Impact simulations with fracture. I. Method and Tests. *Icarus* 107, 98–116.
- Benz, W., Asphaug, E., 1995. Simulations of brittle solids using smooth particle hydrodynamics. *Comput. Phys. Commun.* 87, 253–265.
- Biesiadecki, J.J., Skeel, R.D., 1993. *J. Comput. Phys.* 109, 318–328.
- Bottke, W.F., Nolan, M.C., Greenberg, R., Kolvoord, R.A., 1994. Velocity distributions among colliding asteroids. *Icarus* 107, 255–268.
- Bottke, W.F., Vokrouhlický, D., Brož, M., Nesvorný, D., Morbidelli, A., 2001. Dynamical spreading of asteroid families via the Yarkovsky effect. *Science* 294, 1693–1696.
- Bottke, W.F., Durda, D., Nesvorný, D., Jedicke, R., Morbidelli, A., Levison, H., 2005. The fossilized size distribution of the main asteroid belt. *Icarus* 175, 111–140.
- Britt, D.T., Yeomans, D., Housen, K., Consolmagno, G., 2002. Asteroid density, porosity, and structure. In: Bottke, W.F., Cellino, A., Paolicchi, P., Binzel, P.R. (Eds.), *Asteroids III*. Univ. of Arizona Press, Tucson, pp. 485–500.
- Canup, R.M., 2004. Simulations of a late lunar-forming impact. *Icarus* 168, 433–456.
- Canup, R.M., Asphaug, F., 2001. Origin of the Moon in a giant impact near the end of the Earth's formation. *Nature* 412, 708–712.
- Chapman, C.R., 2004. Space weathering of asteroid surfaces. *Ann. Rev. Earth Planet. Sci.* 32, 539–567.
- Clark, B.E., Hapke, B., Pieters, C., Britt, D., 2002. Asteroid space weathering and regolith evolution. In: Bottke, W.F., Cellino, A., Paolicchi, P., Binzel, R. (Eds.), *Asteroids III*. Univ. of Arizona Press, Tucson, pp. 585–599.
- Duncan, M.J., Levison, H.F., Lee, M.H., 1998. A multiple time step symplectic algorithm for integrating close encounters. *Astron. J.* 116, 2067–2077.
- Durda, D.D., Greenberg, R., Jedicke, R., 1998. Collisional models and scaling laws: A new interpretation of the shape of the main-belt asteroid size distribution. *Icarus* 135, 431–440.
- Durda, D.D., Bottke, W.F., Enke, B.L., Merline, W.J., Asphaug, E., Richardson, D.C., Leinhardt, Z.M., 2004. The formation of asteroid satellites in large impacts: Results from numerical simulations. *Icarus* 170, 243–257.
- Hilton, J.L., 2002. Asteroid masses and densities. In: Bottke, W.F., Cellino, A., Paolicchi, P., Binzel, P.R. (Eds.), *Asteroids III*. Univ. of Arizona Press, Tucson, pp. 103–112.
- Hirayama, K., 1918. Groups of asteroids probably of common origin. *Astron. J.* 31, 185–188.
- Holsapple, K., Giblin, I., Housen, K., Nakamura, A., Ryan, E., 2002. Asteroid impacts: Laboratory experiments and scaling laws. In: Bottke, W.F., Cellino, A., Paolicchi, P., Binzel, P.R. (Eds.), *Asteroids III*. Univ. of Arizona Press, Tucson, pp. 443–462.
- Holsapple, K.A., 2005. Asteroid spin data: No evidence of rubble-pile structures. *Lunar Planet. Sci.* 36. Abstract 2329.
- Jedicke, R., Nesvorný, D., Whiteley, R., Ivezić, Ž., Jurić, M., 2004. An age-colour relationship for main-belt S-complex asteroids. *Nature* 429, 275–277.
- Leinhardt, Z.M., Richardson, D.C., 2002. *N*-body simulations of planetesimal evolution: Effect of varying impactor mass ratio. *Icarus* 159, 306–313.
- Leinhardt, Z.M., Richardson, D.C., 2004. The growth of terrestrial planets: Results from high resolution *N*-body simulations. *AAS/Division for Planetary Sciences Meeting Abstracts* 36, 1176.
- Leinhardt, Z.M., Richardson, D.C., 2005a. Planetesimals to protoplanets. I. Effect of fragmentation on terrestrial planet formation. *Astrophys. J.* 625, 427–440.
- Leinhardt, Z.M., Richardson, D.C., 2005b. A fast method for finding bound systems in numerical simulations: Results from the formation of asteroid binaries. *Icarus* 176, 432–439.
- Leinhardt, Z., Richardson, D.C., Quinn, T., 2000. Direct *N*-body simulations of rubble pile collisions. *Icarus* 146, 133–151.
- Levison, H.F., Duncan, M.J., 2000. Symplectically integrating close encounters with the Sun. *Astron. J.* 120, 2117–2123.
- Love, S.G., Ahrens, T.J., 1997. Origin of asteroid rotation rates in catastrophic impacts. *Nature* 386, 154–156.
- Marzari, F., Davis, D., Vanzani, V., 1995. Collisional evolution of asteroid families. *Icarus* 113, 168–187.
- Melosh, H.J., 1984. Impact ejection, spallation, and the origin of meteorites. *Icarus* 59, 234–260.
- Melosh, H.J., 1989. *Impact Cratering: A Geologic Process*. Oxford Univ. Press, New York.
- Merline, W.J., and 10 colleagues, 2004a. Discovery of binaries among small asteroids in the Koronis dynamical family using the HST Advanced Camera for Surveys. *AAS/Division for Planetary Sciences Meeting Abstracts* 36, 1179.
- Merline, W.J., Tambllyn, P.M., Dumas, C., Menard, F., Close, L.M., Chapman, C.R., Duvert, G., Ageorges, N., 2004b. S/2004 (4674) 1. *IAU Circ.* 8297, 1.
- Michel, P., Benz, W., Tanga, P., Richardson, D., 2001. Collisions and gravitational reaccumulation: A recipe for forming asteroid families and satellites. *Science* 294, 1696–1700.
- Michel, P., Tanga, P., Benz, W., Richardson, D.C., 2002. Formation of asteroid families by catastrophic disruption: Simulations with fragmentation and gravitational reaccumulation. *Icarus* 160, 10–23.
- Michel, P., Benz, W., Richardson, D.C., 2003. Disruption of fragmented parent bodies as the origin of asteroid families. *Nature* 421, 608–611.
- Michel, P., Benz, W., Richardson, D.C., 2004. Catastrophic disruption of pre-shattered parent bodies. *Icarus* 168, 420–432.
- Migliorini, F., Zappalá, V., Vio, R., Cellino, A., 1995. Interlopers within asteroid families. *Icarus* 118, 271–291.
- Murray, C.D., Dermott, S.F., 1999. *Solar System Dynamics*. Cambridge Univ. Press, Cambridge.
- Nesvorný, D., Bottke, W.F., 2004. Detection of the Yarkovsky effect for main-belt asteroids. *Icarus* 170, 324–342.
- Nesvorný, D., Bottke, W.F., Levison, H., Dones, L., 2002. A recent asteroid breakup in the main belt. *Nature* 417, 720–722.
- Nesvorný, D., Bottke, W.F., Levison, H.F., Dones, L., 2003. Recent origin of the Solar System dust bands. *Astrophys. J.* 591, 486–497.
- Nesvorný, D., Jedicke, R., Whiteley, R.J., Ivezić, Ž., 2005. Evidence for asteroid space weathering from the Sloan Digital Sky Survey. *Icarus* 173, 132–152.
- Richardson, D.C., Quinn, T., Stadel, J., Lake, G., 2000. Direct large-scale *N*-body simulations of planetesimal dynamics. *Icarus* 143, 45–59.
- Richardson, D.C., Leinhardt, Z.M., Melosh, H.J., Bottke, W.F., Asphaug, E., 2002. Gravitational aggregates: Evidence and evolution. In: Bottke, W.F., Cellino, A., Paolicchi, P., Binzel, P.R. (Eds.), *Asteroids III*. Univ. of Arizona Press, Tucson, pp. 501–515.
- Richardson, J.E., Melosh, H.J., Greenberg, R., 2004. Impact-induced seismic activity on Asteroid 433 Eros: A surface modification process. *Science* 306, 1526–1529.
- Richardson, D.C., Elankumaran, P., Sanderson, R.E., 2005. Numerical experiments with rubble piles: Equilibrium shapes and spins. *Icarus* 173, 349–361.
- Rubincam, D.P., 2000. Radiative spin-up and spin-down of small asteroids. *Icarus* 148, 2–11.
- Sasaki, T., Sasaki, S., Watanabe, J., Sekiguchi, T., Yoshida, F., Kawakita, H., Fuse, T., Takato, N., Dermawan, B., Ito, T., 2004. Mature and fresh surfaces on the newborn Asteroid Karin. *Astrophys. J.* 615, L161–L164.
- Sasaki, T., Sasaki, S., Watanabe, J.I., Sekiguchi, T., Yoshida, F., Ito, T., Kawakita, H., Fuse, T., Takato, N., Dermawan, B., 2005. Difference in degree of space weathering on the newborn Asteroid Karin. *Lunar Planet. Sci.* 36. Abstract 1590.

- Scott, E.R.D., Wilson, L., 2005. Meteoritic and other constraints on the internal structure and impact history of small asteroids. *Icarus* 174, 46–53.
- Stadel, J., 2001. Cosmological  $N$ -body simulations and their analysis. Thesis. University of Washington, Seattle, 126 pp.
- Sullivan, R.J., Thomas, P.C., Murchie, S.L., Robinson, M.S., 2002. Asteroid geology from Galileo and NEAR Shoemaker data. In: Bottke, W.F., Cellino, A., Paolicchi, P., Binzel, R. (Eds.), *Asteroids III*. Univ. of Arizona Press, Tucson, pp. 331–350.
- Tamblyn, P.M., Merline, W.J., Chapman, C.R., Nesvorný, D., Durda, D.D., Dumas, C., Storrs, A.D., Close, L.M., Menard, F., 2004. S/2004 (17246) 1. *IAU Circ.* 8293, 3.
- Tanga, P., Cellino, A., Michel, P., Zappalà, V., Paolicchi, P., Dell’Oro, A., 1999. On the size distribution of asteroid families: The role of geometry. *Icarus* 141, 65–78.
- Tedesco, E.F., Noah, P.V., Noah, M., Price, S.D., 2002. The supplemental IRAS minor planet survey. *Astron. J.* 123, 1056–1085.
- Tillotson, J.H., 1962. Metallic equations of state for hypervelocity impact. General Atomic Report GA-3216.
- Vernazza, P., Fulchignoni, M., Birlan, M., Dotto, E., Rossi, A., Fornasier, S., Marzari, F., Nesvorný, D., 2005. Spectroscopic characterization of the Karin family. *AAS/Division for Planetary Sciences Meeting Abstracts* 37, 644.
- Vokrouhlický, D., Nesvorný, D., Bottke, W.F., 2003. The vector alignments of asteroid spins by thermal torques. *Nature* 425, 147–151.
- Wisdom, J., Holman, M., 1991. Symplectic maps for the  $N$ -body problem. *Astron. J.* 102, 1528–1538.
- Yoshida, F., and 16 colleagues, 2004. Photometric observations of Karin family asteroids. In: *Asteroid Dynamics Workshop*. Arecibo Observatory, Arecibo, Puerto Rico.
- Zappalà, V., Cellino, A., Farinella, P., Milani, A., 1994. Asteroid families. II. Extension to unnumbered multiopposition asteroids. *Astron. J.* 107, 772–801.
- Zappalà, V., Cellino, A., dell’Oro, A., Paolicchi, P., 2002. Physical and dynamical properties of asteroid families. In: Bottke, W.F., Cellino, A., Paolicchi, P., Binzel, P.R. (Eds.), *Asteroids III*. Univ. of Arizona Press, Tucson, pp. 619–631.